UNIVERSITÀ DEGLI STUDI DI PADOVA

Dipartimento di Ingegneria dell'Informazione

A.A. 2022/2023

Corso di Laurea Magistrale in Ingegneria Elettronica

Development of an active EMI filter for CM conducted emissions and comparison with an integrated solution

Sviluppo di un filtro attivo EMI per emissioni condotte CM e confronto con una soluzione integrata

UNIVERSITÀ DEGLI STUDI DI PADOVA

DIPARTIMENTO DI INGEGNERIA DELL'INFORMAZIONE

Relatore
prof. Buso Simone

Laureando:
Corrent Daniel

30 Novembre 2023

Thanks to my family and my friends

Abstract

Technological advances in recent decades have led to incredible increases in performance and power density in electronic converters. On the other hand, passive components and conducted emission filtering systems have not seen a similar level of development. This fact has made the size of EMI filters more and more relevant and, currently, they can occupy more than one third of an electronic board, thus representing one of the main limitations in the compactness of an electronic system.

Active filtering systems are one proposal in trying to overcome this problem. This document presents the development of an active EMI filter for filtering common-mode conducted emissions, discussing in depth its choice of topology, design, and performance in different practical cases. Nevertheless, issues limiting applications of this technology are also considered. The results obtained are then compared with those obtained by employing a commercially available integrated solution.

In addition, the development of a system capable of separating common-mode and differential-mode noise, employed in the experimental evaluation of the performance of the EMI filters mentioned above, will also be discussed.

Sommario

I progressi tecnologici degli ultimi decenni hanno portato ad un incredibile incremento delle prestazioni e della densità di potenza nei convertitori elettronici. Dal canto loro, i componenti passivi e i sistemi di filtraggio delle emissioni condotte non hanno visto un livello di sviluppo analogo. Questo fatto ha reso le dimensioni dei filtri EMI sempre più preponderanti ed attualmente possono arrivare ad occupare anche più di un terzo di una scheda elettronica, rappresentando quindi uno dei principali limiti nella compattezza di un sistema elettronico.

I sistemi di filtraggio attivi costituiscono una delle proposte per cercare di superare questo problema. In questo elaborato viene presentato lo sviluppo di un filtro EMI attivo per il filtraggio delle emissioni condotte di modo comune, discutendone approfonditamente la scelta della topologia, il dimensionamento e le prestazioni in diversi casi pratici. Nondimeno, vengono anche considerate le problematiche che limitano le applicazioni di questa tecnologia. I risultati ottenuti sono poi stati confrontati con quelli ottenuti impiegando una soluzione integrata disponibile commercialmente.

In aggiunta, verrà anche discusso lo sviluppo di un sistema in grado di separare i disturbi di modo comune e differenziale, impiegato nella valutazione sperimentale delle prestazioni dei filtri EMI citati in precedenza.

Contents

List of Figures

Chapter 1

Introduction

As well known, the technological progress of recent decades has led to an exponential diffusion of electronic devices which, also driven by the electrification race of recent years (and currently underway), now dominate any application. From home appliances, to automobiles, to communications, to energy management, it is hard to find an area where electronics has not taken over. The expansion of this "population", however, requires the definition of rules of coexistence, to prevent scenarios in which the presence of one device compromises the operation of another.
This is where a branch of electronics called electromagnetic compatibility (EMC) comes into play, which defines a set of limits, standards and tests related to various scopes, that aim to regulate the electromagnetic pollution and ensure the coexistence of all the devices around us. Therefore, during the design of each electronic circuit it becomes necessary to dedicate a section of the board and part of the design efforts to verify and guarantee compatibility with these "coexistence rules".

However, recently, these circuits (traditionally implemented with passive elements) are representing a critical point in the development of electronic devices, in particular from the point of view of compactness and energy density. Indeed, there is no doubt that active components such as switches and integrated circuits have seen frightening progress in recent years, enabled by the development of new technologies and processes. To be convinced of this, it is sufficient to observe the level of integration achieved by the latest integrated circuits or the switching speed and power manageable by recent switches based on SiC and GaN and compare them with devices from just 10 years ago.

Unfortunately, the same cannot be said for passive components, with which the filters for electromagnetic emissions are made, whose performance remained almost unchanged. Consequently, while the size of the functional part of the circuit continued to reduce, thanks to these new technologies, the part dedicated to electromagnetic compatibility maintained its size and, at the moment, it can occupy even a third of the board of an electronic circuit, representing a great limit in the development of the compactness and energy density of an electronic converter or a device in general. For this reason, great efforts have recently been made to identify techniques and technologies that would allow us to overcome this limitation. Many of these act on the origin of the disturbances. Others suggest solutions that try to improve the performance of passive filters. Others propose alternative approaches, based on the compensation of disturbances by means of an active circuit.

In this work this latter approach has been explored and analysed, with the aim of introducing this system into a photovoltaic grid-connected inverter. The purpose of this thesis is to evaluate the effectiveness, advantages and limitations of this solution and determine the feasibility of introducing it into a commercial device of this type.

This work is divided into 3 main chapters:

- in Chapter 2 a quick presentation and some recalls of the concept of conducted emissions are made. The origin and propagation methods of conducted disturbances are described and traditional mitigation methods are presented, highlighting their pros and cons.
- in Chapter 3, after a brief introduction, the development of an active EMI filter is presented. The various design choices are justified and an extensive analysis of the system is made. This circuit was then physically implemented and the performance was evaluated on several practical cases. The homemade system is also compared with a similar, commercially available, plug and play integrated solution.
- in Chapter 4 the design, analysis and test of a device capable of separating differential mode and common mode signals is described. This is intended to be introduced in an EMI evaluation setup and resulted useful also in the AEF analysis.

Chapter 2

Conducted emissions in power converters

2.1 Basic concepts

Nowadays even the simplest electronic devices are made up of very sophisticated circuits, which can include multiple sections that fulfill different functions. We can find energy conversion stages, digital and analog signal processing, wireless communication, motor driving, etc. For the reasons that will be described later, the disturbances produced by these devices rarely remain contained within the device itself and can propagate both through cables and through the air, potentially disturbing or compromising the functionality of other devices. To prevent problems of this type, various regional and international organizations such as IEC, CISPR and FCC have set regulations, limits and standards for this purpose, which must be respected by every product that wants to be commercialized.
The area of EMC and these regulations are divided into two main categories, identified as EMI and EMS (Figure 2.1): The term electromagnetic interferences (EMI) refers to disturbances that are unintentionally generated by a device and propagate outside of it. On the other hand, the term Electromagnetic Susceptibility (EMS), refers to the ability of a device to maintain a certain level of operation even in the presence of disturbances or stresses from the outside.
These are then complemented by various safety-related regulations.

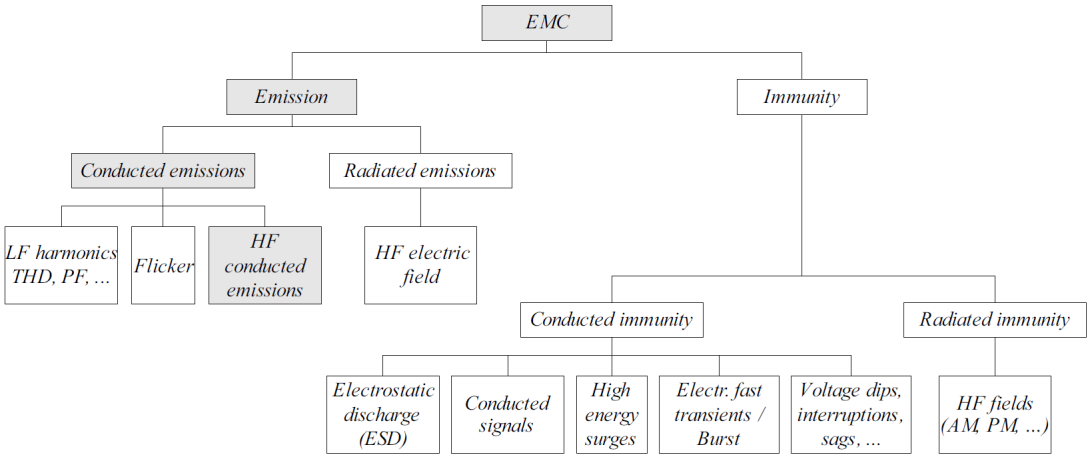

Figure 2.1: EMC fields hierarchy [10].

In this work we will focus on the concept of electromagnetic emissions and, in particular, on conducted emissions. In fact, electromagnetic compatibility regulations distinguish the disturbances generated by a device depending on their frequency (Figure 2.2):

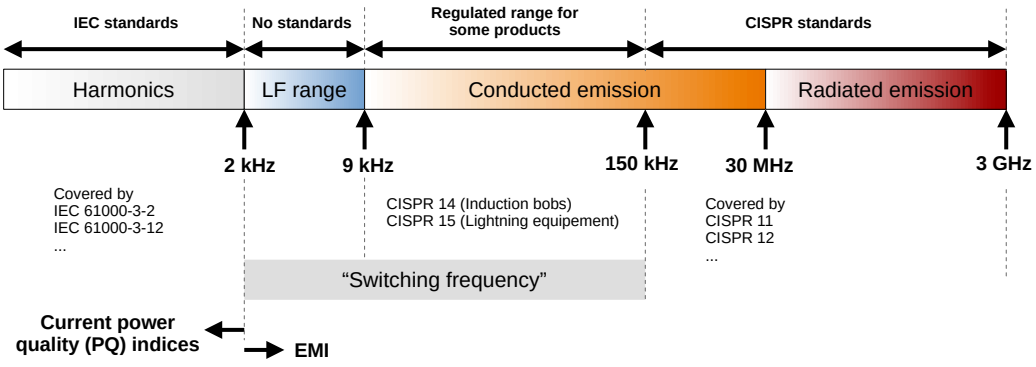

Figure 2.2: Harmonic and EMI frequency ranges classified by IEC [3].

- *Low frequency emissions*: Disturbances at frequencies lower than $150kHz$, which therefore include also harmonics of the line frequency
- *Conducted emissions*: Disturbances at frequencies included between $150kHz$ and $30MHz$. These signals are characterized by the fact that they propagate

through cables and physical connections. In certain applications the lower end of this range is extended down to $9kHz$.

- *Radiated emissions*: Disturbances at frequencies greater than $30MHz$. At this frequency level the wavelength is typically sufficiently small to become comparable with the circuit dimensions, therefore they can propagate in the air reaching nearby devices.

Finally, let's recall the main methodology employed in the conducted emissions evaluation (as specified in *CISPR-16* regulations), that will be often considered in this document *i.e.* the LISN (Line Impedance Stabilization Network). This device is typically introduced between the DUT and the grid and performs two main functions: it isolates and extract the conducted interferences generated by the DUT (which can then be visualized on a spectrum analyzer) and it normalizes the impedance seen by the DUT on the grid-side [1].

2.2 Origin of EMI in power converters

In any electronic device, the main cause of the generation of EMI noise is the repeated and rapid commutation of voltage and current signals. In fact, these can generate high frequency components that easily fall within the range of electromagnetic interference and which can easily find a path to propagate outside the device. It can be deduced, therefore, that the main culprits of EMI generation will be digital circuits and, especially, power converters. The latter, in fact, base the principle of their operation on the switching of large levels of voltage and current, with increasingly higher frequencies (tens or hundreds of kHz).
In every converter it is possible to identify at least one node on which this occurs, called the switching node. If we consider a buck converter as in Figure 2.3(a) (but this reasoning can be applied to any other type of converter) the switching node can be easily identified. The signals involved exhibit the classic trapezoidal shape (Figure 2.3(b)), with edges whose slopes can even reach $50kV/\mu s$ or $1000A/\mu s$. This aspect is the basis of their efficiency, but can be very problematic from an EMI point of view, considering the extremely broad spectrum that these signals present [4].
This becomes evident if the parasitic parameters of the system are taken into account. In particular, it is essential to consider the series inductance of the input

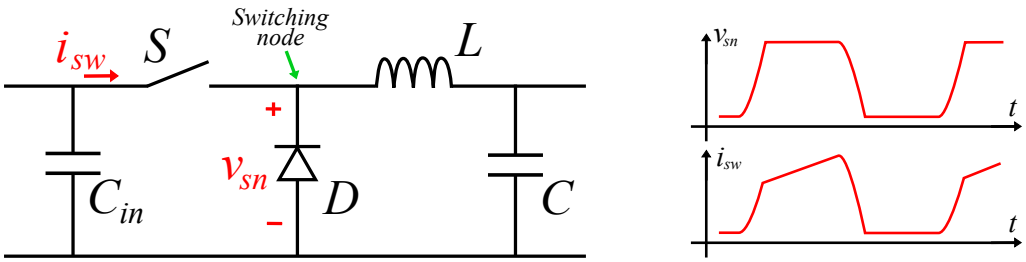

(a) (b)

Figure 2.3: (a) A simple buck converter where the switching node has been highlighted. (b) The typical waveform shapes in a converter.

capacitor C_{in}. Indeed, this is typically a large electrolytic capacitor, that, consequently, will definitely present a considerably low self-resonance frequency (tens of kHz). This means that, as far as the EMI frequency range is concerned, this capacitor will be completely ineffective and will rather show inductive behavior. As a result, the high-frequency components of the current signal at the switching node will be free to propagate out of the converter.
The other element that must be taken into consideration is the parasitic coupling capacitance towards ground of the switching node (which is typically created between the backside of the switch and the heat sink). Since there are rapid voltage variations at this node, this element creates another path through which disturbances can propagate out of the converter.

Therefore, an equivalent model valid for EMI frequencies can be drawn (Figure 2.4). From this model it becomes evident that the current generator contributes for Differential Mode (DM) noise, while the voltage one contributes for Common Mode (CM) noise [1].

In this paragraph, the main causes with which EMI disturbances are generated and propagated in a power converter have been presented, in a sufficient way for the purposes of this thesis. Anyway, in [7] a much more precise analysis has been made, which aims to explain in detail the various processes and contributions that participate in forming the spectrum of EMI disturbances that can be detected on the output. In particular, a much more refined model of the circuit is considered, which tries to characterize the effect of most of the parasitic elements of the circuit, such

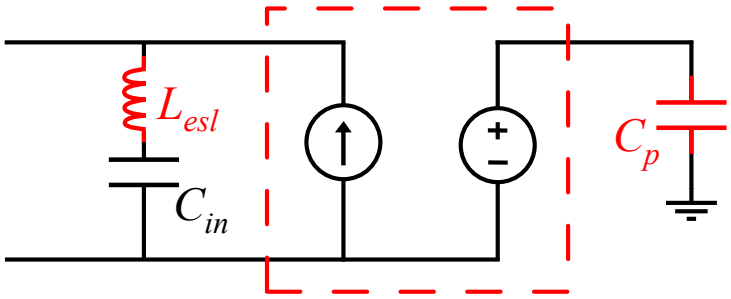

Figure 2.4: The equivalent model from the EMI point of view, that highlights noise sources and coupling paths. L_{esl} is the equivalent series inductance of the input capacitor, while C_p is the equivalent coupling capacitance toward PE.

as the capacitances of the switches, the parasitic inductances of the connections, the parasitic elements of the passive components and other modes of capacitive coupling to ground. A deep analysis of the electromagnetic perturbations caused by bonding connection and by the PCB has also been done. This highlights both new possible sources of noise, given by ringing and resonances between parasitic capacitances and inductances, and new paths through which disturbances can propagate, allowing an extremely accurate characterization of the noise produced by a device.

2.3 Conducted emissions mitigation techniques

To cope with this problem and enable devices to be marketed while complying with regulations, several techniques have been developed. Basically, these techniques can act in 2 ways:

- Intervene on the source of the disturbance
- Intervene on the path followed by the disturbances

Intervening on the source includes a series of techniques that aim to prevent the generation of high frequency disturbances. In fact, it is possible to act on the degrees of freedom of a system to implement different switch control methodologies that allow the electromagnetic impact to be reduced. For instance, among these techniques we find: lowering of the switching frequency, switching frequency modulation (spread spectrum techniques), employment of snubbers, commutations speed reduction, exploitation of soft commutations [20]. Sometimes an EMI improvement

can be achieved just rearranging the circuit layout, in order to optimize the critical connections that are responsible for the the most impactful parasitic components (for instance, a good layout is achieved when the circuit loops interested by large impulsive currents are physically kept as small as possible, in order to minimize their inductance and ringing), or even improving component selection (for instance preferring SMD packages or toroidal cores).

Often, these solutions are not implementable or are not sufficient to reduce the disturbances to an acceptable level. Therefore, a different approach that aims to intercept electromagnetic interference along their path have to be considered. The most widespread solution is based on EMI filters.
Traditional EMI filters use passive components like capacitors and inductors to realize alternative paths which do not allow disturbances to propagate outside the device. The most suitable topology should be determined depending on the considered device, however, the most common structure has been reported in Figure 2.5.

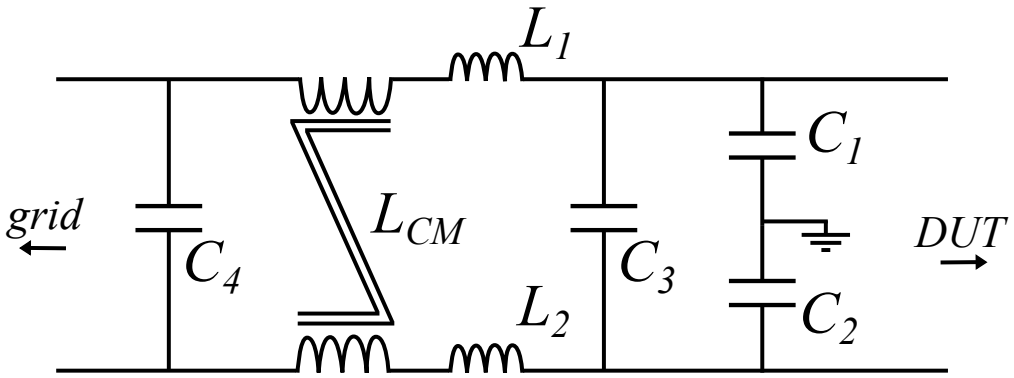

Figure 2.5: Typical structure of a Passive EMI Filter.

Here CM and DM signals are handled separately, in fact this circuit can be seen as the combination of the two filters of Figure 2.6 , that corresponds to a π-filter (for DM noise) and a CL-filter (for CM noise).

These filters are realized using specific components:

- C_1 and C_2 are Y-Capacitors

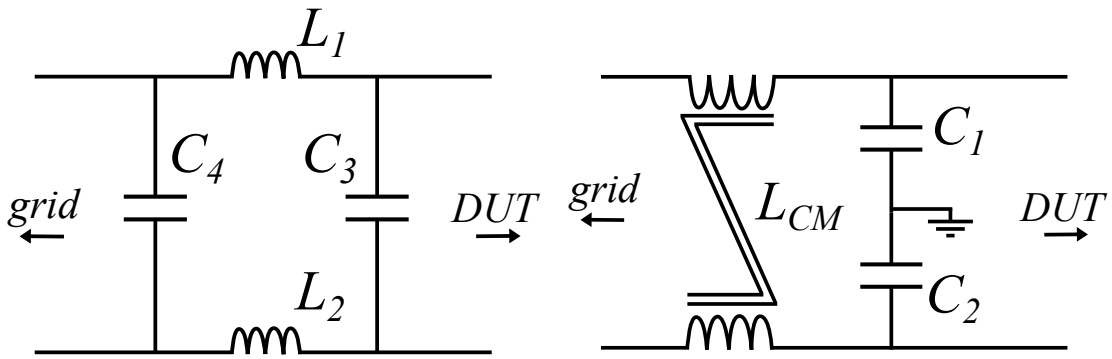

Figure 2.6: (a) The equivalent circuit seen by DM noise and (b) that seen by CM noise.

- C_3 and C_4 are X-Capacitors
- L_{CM} is a CM-choke, i.e. a particular type of inductor which (ideally) shows very high inductance for CM signals and zero inductance for DM signals
- L_1 and L_2, usually, are not actual components but they are implemented exploiting the leakage inductances of the CM-choke

X and Y capacitors are characterized to eventually fail in a predefined way (respectively, as a short and as an open circuit) for safety reasons. In addition, they are able to withstand very large voltage transients.

Passive EMI filters have the advantages to be very simple, robust and reliable. Moreover, they are also very versatile and scalable. However, as already discussed, they have also the great defect to be very bulky and heavy.
This is due to the fact that safety recommendations limit the maximum allowed leakage current through Y-capacitors and therefore also their maximum value. As a consequence, the only way to achieve high CM attenuation is by introducing a very large CM-choke (or introducing more stages). However, as this device has to carry the whole input current, the windings should be realized using a very thick wire and, in order to avoid saturation, a very big toroidal core is necessary. This makes the sizes of this object very demanding. In addition, also the dimensions of X-capacitors could be not negligible in some situations. Obviously, this aspect becomes more and more relevant as the power managed by the device grows.

Note also that the larger the component, the larger its stray effects, therefore achieving good attenuation also for the higher end of the EMI spectrum could become difficult.

Hence, much effort has been put into finding solutions to this problem. In this context, some strategies that help in reducing passive EMI filter sizes have been proposed, like planar electromagnetic bandgap structures or passive cancellation strategies [25].
Another promising proposal are Active EMI Filters (AEF). This solution aims to sense and compensate EMI disturbances by means of an active circuit. As it showed the capability to achieve very good performance in many situations, this approach will be deeply evaluated and analyzed in the next chapter.

Chapter 3

Active EMI filter design and comparison

As described in Chapter 2, EMI filters currently represent a bottleneck in the growth of power density and compactness in power converters. To overcome these limits many alternative techniques have been developed, which aim to improve filter effectiveness or to reduce EMI generation.
In this chapter, the approach based on active EMI filters is considered. After a brief introduction, the design process of a CM Active EMI Filter is presented. Then, its performance will be evaluated and compared with those of an integrated solution. The goal of this study is to determine the feasibility to introduce this approach in the output stage of a commercial grid-connected photovoltaic inverter. Therefore, the advantages and, mostly, the limits of this approach will be carefully addressed.

3.1 Active EMI filters: general concept

In this section, a brief introduction on the concept of AEF is given. The basic structure and the principle of operation is presented. Thereafter, the available topologies and their pros and cons will be discussed.

3.1.1 Basic structure

Intuitively, active EMI filters operate differently from passive ones: in fact, typical passive filters exploit reactive components to arrange an high frequency path along

which the EMI noise is redirected to the source that generated it, preventing it from leaving the device. In active filters, instead, the noise signal is probed by a sensing stage, processed and then injected back into the circuit in order to compensate the unwanted signal.

Therefore, active filters are usually composed by three basic parts:

- the *noise-sensing* circuit is used to detect the noise. Different types of sensing structures can be distinguished, depending on the desired effect. In fact, the presence of the noise can be evaluated either by looking at the current or at the voltage signal. Therefore, the four main configurations are reported in Figure 3.1.
  Current sensing is usually implemented with a current transformer, structure (a) is used for CM and structure (b) for DM. On the other hand, voltage sensing is done using capacitors, where structures (c) and (d) are respectively used for CM and DM.

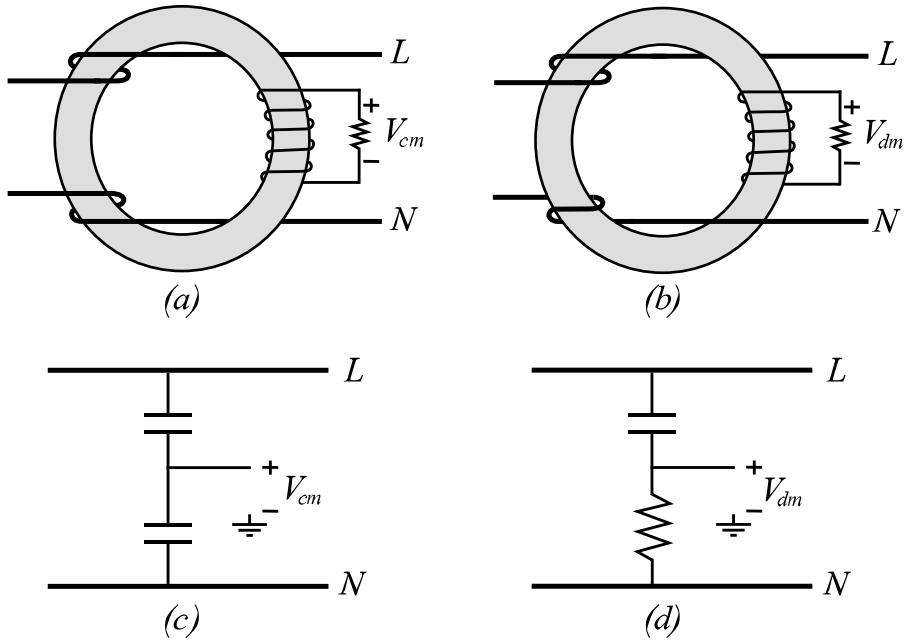

Figure 3.1: The 4 main sensing typologies: (a) CM current sensing, (b) DM current sensing, (c) CM voltage sensing, (d) DM voltage sensing.

- the *noise-processing* active circuit is used to amplify, filter and elaborate the

sensed signal. It can be implemented in different ways, such as using operational amplifiers or discrete components (*e.g.* push-pull amplifiers), according to the required performance and structure. Op-Amps offer more degrees of freedom during the design stage, whereas push-pull structures are cheaper and more robust against high voltage transients (*e.g.* surges). Also digital processing techniques involving DSP or FPGA have been experimented [17].

- the *noise-injection* circuit injects the compensation signal. Again, different structures can be identified and are distinguished according to the type of injection (voltage or current) and noise mode (DM or CM) that has to be eliminated. Similar topologies of those of Figure 3.1 are used, with the fundamental difference that now capacitors are used for current injection and transformers are used for voltage injection, as represented in Figure 3.2.

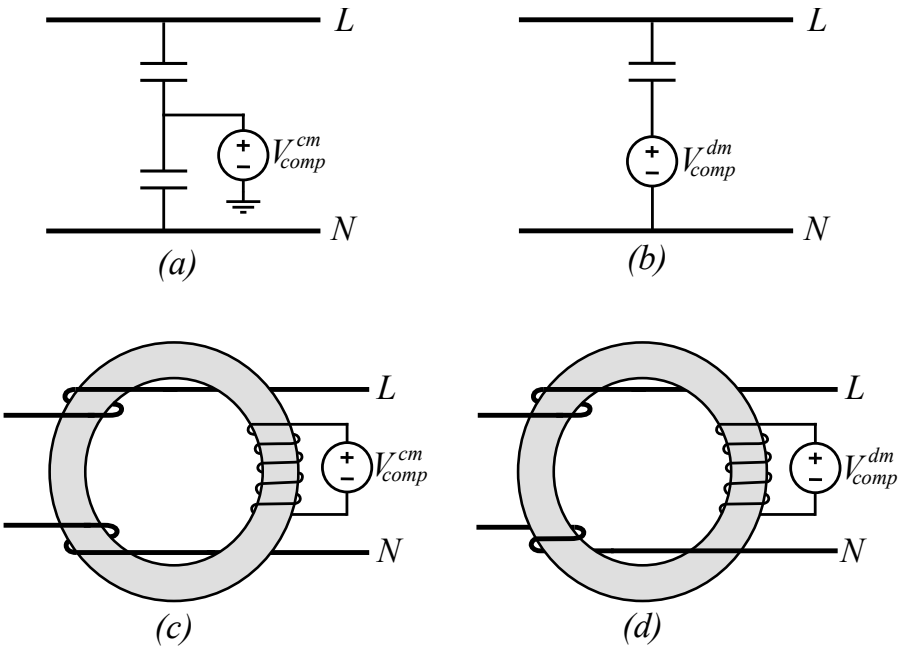

Figure 3.2: The 4 main compensation typologies: (a) CM current injecting, (b) DM current injecting, (c) CM voltage injecting, (d) DM voltage injecting.

Active EMI filters can be realized either implementing *feedback* or *feedforward* structures. In the first case, the noise is sensed close to the load and the compensation signal is injected at the source, thus realizing an high gain feedback loop, that tends to attenuate the noise. The feedforward topology, instead, senses the noise

close to its source and injects an identical signal with opposite phase, that cancels the noise.

In conclusion, considering the various combinations of sensing and injection, 4 feedback and 2 feedforward typologies can be recognized, summarized in Figure 3.3.

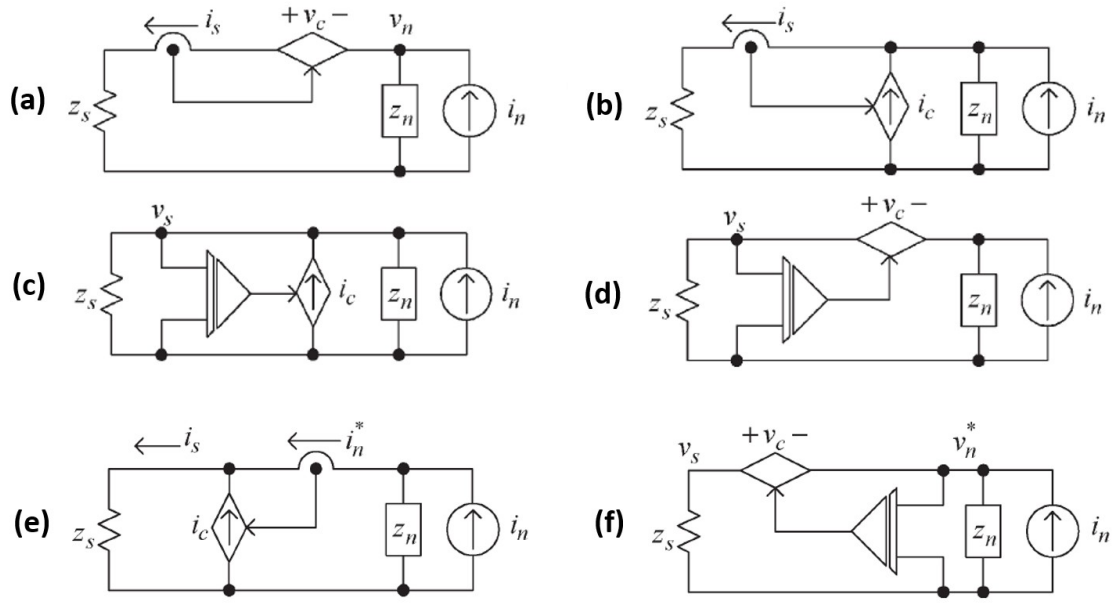

Figure 3.3: Feedback type active filters: (a) Current detecting and voltage compensating (type I). (b) Current detecting and current compensating (type II). (c) Voltage detecting and current compensating (type III). (d) Voltage detecting and voltage-compensating (type IV). Feedforward type active filters: (e) Current detecting and current compensating (type V). (f) Voltage-detecting and voltage-compensating (type VI) [27].

3.1.2 Topologies characteristics

One of the main parameters that characterize the performance of an EMI filter is the *Insertion Loss* (IL), defined as:

$$IL = \frac{V_{LWO}}{V_{LW}} , \tag{3.1}$$

where V_{LWO} is the voltage on the load without the filter and V_{LW} is that with the filter.
In a certain way, this parameter quantifies the noise reduction capabilities of an EMI filter. The higher IL, the higher the noise attenuation, hence it should be maximized.

The insertion losses provided by each structure described in the previous section can be easily computed and are reported in Table 3.1, where z_s and y_s are the impedance and admittance of the load, z_n and y_n those of the noise source and A is the gain of active stage.

Type	Amplifier type and gain	Insertion loss (IL)	Condition for maximum IL
I	Trans-impedance $v_c = -A_1 i_s$	$1 + \frac{A_1}{z_s + z_n}$	$A_1 \gg z_s + z_n$
II	Current gain (FB) $i_c = -A_2 i_s$	$1 + \frac{z_n}{z_s + z_n} \cdot A_2$	$z_n \gg z_s$
III	Trans-admittance $i_c = -A_3 v_s$	$1 + \frac{A_3}{y_s + y_n}$	$A_3 \gg y_s + y_n$
IV	Voltage gain (FB) $v_c = -A_4 v_s$	$1 + \frac{z_s}{z_s + z_n} \cdot A_4$	$z_s \gg z_n$
V	Current gain (FF) $i_c = -A_5 i_n^*$	$\left(1 + \frac{1}{1 - A_5}\right)\left(1 - \frac{A_5 z_s}{z_s + z_n}\right)$	$A_5 = 1, z_n \gg z_s$
VI	Voltage gain (FF) $v_c = -A_6 v_n^*$	$\left(1 + \frac{1}{1 - A_6}\right)\left(1 - \frac{A_6 z_n}{z_s + z_n}\right)$	$A_6 = 1, z_s \gg z_n$

Table 3.1: Amplifier description and insertion loss of the 4 feedback and 2 feedforward topologies [27].

Looking at Table 3.1 it can be observed that IL strongly depends on the amplifier gain and also on the values of the source and load impedances. Thus, the most suitable topology should be determined accordingly.

It can be noticed that when there is a large mismatch between z_s and z_n, the insertion losses of topologies II and IV depend only on the gain of the amplifier.

Hence, topology II should be considered when the noise source behaves like an ideal current source (with infinite internal impedance) and, conversely, topology IV should be considered when the noise source behaves like an ideal voltage source (with zero internal impedance). Thus, in this cases, to achieve high IL, it's sufficient to provide high gain A.
On the other hand, the performance of structures I and III would be strongly dependent on z_s and z_n. Indeed, a type I filter introduced in a system with *very high* noise source impedance would be ineffective [2] [27].
In real applications z_s and z_n are difficult to be precisely determined. However, in general terms, we can say that CM disturbances usually show an high impedance source (as it is originate by capacitive couplings toward earth), while DM noise shows a low impedance source (the reservoir capacitance)[18]. Therefore, topology II is recommended for CM suppression and topology IV for DM [5].

The other two topologies shouldn't be discarded anyway. Type-I filters, indeed, uses transformers for both sensing and compensation. This is good in terms of robustness and safety. However transformers should be placed along power lines, making them heavy, bulky (Figure 3.4) and susceptible in terms of saturation and distortion.
Type-III filters are implemented using capacitors for both sensing and injecting.

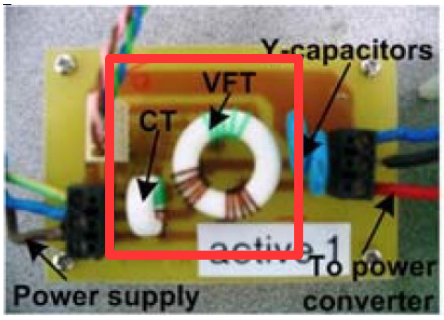

Figure 3.4: Type-I active EMI filter: as can be seen, the sensing current transformer and the injecting voltage transformer totally determine the size of filter [18].

This makes them the most compact solution, but they could still present safety-related limitations.

Regarding feedforward topologies V and VI, it can be noticed that insertion

losses tend to infinity when the amplifier gain is equal to 1. However, in practice, it is hard to obtain this exact value, so it is still useful to maximize the mismatch between z_s and z_n, as done for topologies II and IV [27].

3.2 Discrete Active EMI Filter Design

In this section the development of a discrete Active EMI Filter (AEF) for compensation of common mode conducted emissions will be presented.
Firstly, the topology selection is largely discussed, taking into account all the system requirements. Then, a deep analysis and development of the considered structure has been conducted. Thereafter, the effectiveness of the final system has been evaluated through simulations and, finally, the circuit has been implemented on a PCB.

3.2.1 Topology selection

The first step of the Active EMI Filter (AEF) design is the selection of the topology. As discussed in section 3.1 several structures are available and the most suitable one for our application should be chosen.

Firstly, a distinction between *feedback* and *feedforward* structures should be done. As already said, feedforward structures can show very good performance if their amplifier stage presents unitary gain. However, in practice, it is hard to meet this condition, due to the stray components of the sensing and injecting networks which enhance the uncertainty of this parameter. Moreover, in this case, filter performance would be strongly related to the components accuracy.
On the other hand, feedback configuration allows to achieve good performance just by maximizing the gain of the active stage. Therefore, *feedback* topology has been considered in this work.

Secondly, the methodologies to implement either the sensing and injecting networks have to be defined. Considering the reasoning done at the end of Section 3.1.2 we could conclude that the best configuration for CM compensation is Type II (current sensing/current injecting), as it probably would show the highest insertion

losses in our case. However, many other considerations should be done.
Current sensing and voltage injection are both implemented using transformers (Figure 3.1 and Figure 3.2). Transformers have the advantage to be very robust against faults and naturally offer an isolated structure which does not present any leakage current toward protection earth, avoiding safety issues. However, these elements should offer a very large bandwidth, therefore many precautions have to be taken during their realization in order to minimize stray effects (winding capacitance and self resonances) which could compromise the AEF performance. In addition, they have to be placed along the power line path, hence their windings should be able to carry the full current of the DUT. All these aspects make coupling transformers heavy, bulky and susceptible in terms of saturation and distortion. To limit the volume occupation, one might consider to put an additional sensing winding in an already existing CM-choke. Unfortunately, this solution did not show good results [11]. Hence, transformers represent a limit on the compactness achievable with an AEF and also their cost would not be negligible. In addition, by their nature, the characteristics are also very sensitive to the way they are constructed and positioned, making the overall performance of the AEF less predictable and, more importantly, not repeatable, unless the method of construction is further complicated.
On the other hand, voltage sensing and current injection are implemented using capacitors. Capacitors have the fundamental drawback to cause leakage currents toward protection earth, therefore their maximum value is limited by specific safety regulations. For this reason also the maximum achievable performance using capacitive coupling is limited. Nevertheless, capacitors are cheaper, lighter and less affected by parasitics compared to transformers. In addition, their compact shape allows to achieve the maximum size reduction. It is often mentioned the fact that they could fail due to overvoltages or electrical overstress, realizing low impedance path or shortcircuits that could endanger the rest of the circuit or safety. However, this issue could be overcome selecting appropriated Y-safety rated capacitors.

In conclusion, recalling the purposes of this study, we want to evaluate the feasibility to introduce an active EMI filtering solution in a commercial device. As a consequence, *reliability*, *cheapness* and especially *repeatability* are key features for our project. Therefore, a solution fully based on capacitors has been selected, hence a feedback Voltage Sensing Current Compensation (VSCC) topology will be

considered in this work.

3.2.2 Selected topology analysis

The basic structure of the adopted topology is reported in Figure 3.5. As shown in this figure, the active block has been implemented using an operational amplifier, owed to its versatility and optimization compared to other solutions based on discrete amplifiers. This OpAmp should present sufficient Gain-Bandwidth Product (GBP) to provide the required gain in the EMI frequency range and, at the same time, it should provide enough output current to drive the injection circuit.

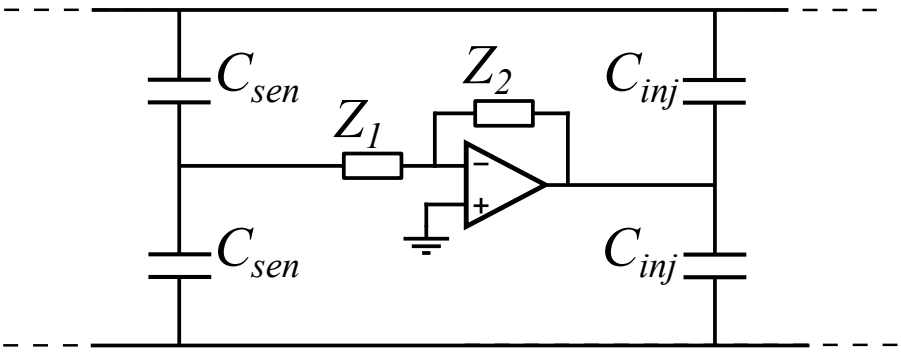

Figure 3.5: Basic structure of a Voltage Sensing Current Compensation topology.

VSCC structure compensates the sensed noise by injecting (or absorbing) a current ideally equal to that which generated it. In other words it realizes a very low impedance path along which conducted noise is redirected to its origin, as a capacitor would do.
Indeed, the idea behind this circuit is to exploit the effect of the active circuit to simulate a capacitor of much higher capacitance than the one actually mounted. By properly modelling the frequency response of the inner amplifier we can introduce this effect just in the frequency range where it is actually needed, avoiding causing issues related to leakage currents at line frequency. In this way we can "virtually" mount Y-capacitors with much larger capacitance than the maximum allowed by regulations.

To better analyze the considered structure, it can be useful to represent the circuit from the point of view of CM disturbances. Considering their symmetrical behavior with respect to protection earth (due to the way they are defined), it is possible to take the PE potential as a reference and work just on an half equivalent circuit. In order to obtain this equivalent circuit it is sufficient to halve the injection and sensing impedances, as reported in Figure 3.6.

Z_{lisn} represents the effective impedance seen by the equivalent circuit on the grid

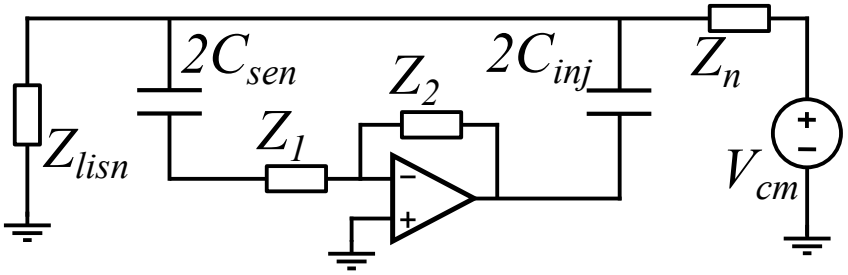

Figure 3.6: CM equivalent circuit of the VSCC structure.

side. In the evaluation of conducted disturbances, this impedance is defined by the LISN, that normalizes and standardizes this value. Its behavior as a function of frequency is established by regulations (CISPR-16-1) and, looking at the conducted emissions frequency range ($150kHz - 30MHz$), it can be considered almost constant with a value around 50Ω. As this impedance is applied on each line and since, from CM disturbances point of view, they appear in parallel, we can conclude that in our CM equivalent circuit $Z_{lisn} \simeq 25\Omega$.

On the other side of the AEF, the DUT has been simplified with the equivalent Thevenin representation of a CM noise source. Z_n represents the noise source impedance, which, as described in Section 2.2, will be mostly capacitive.

An accurate study of this circuit can be done by redrawing the structure proposed in Figure 3.6 like in Figure 3.7.

In this way the presence of an inner amplifier and of an external additional feedback (realized by the injection capacitance) becomes evident.

The main parameter that allows to evaluate the effectiveness of the active filter is its input impedance Z_{AEF}.

In order to compute that, firstly the transfer function of the inner amplifier $G_{in}(s)$

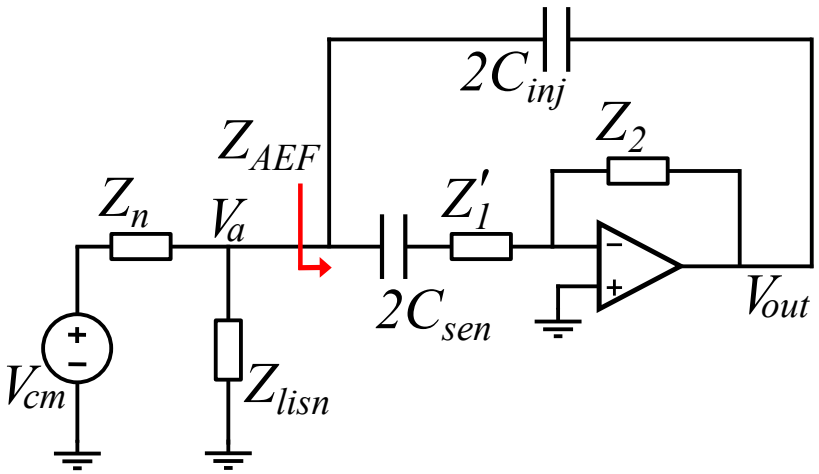

Figure 3.7: CM equivalent circuit of the AEF, redrawn highlighting the dual feedback.

is derived:

$$G(s) \triangleq \frac{V_{out}}{V_a} = -\frac{Z_2}{Z_1} \ , \qquad \text{where: } Z_1 \triangleq Z_1' + Z_{sen} \triangleq Z_1' + \frac{1}{s \cdot 2C_{sen}} \ . \tag{3.2}$$

Now, applying Miller's theorem, the injection impedance $Z_{inj} = \frac{1}{s \cdot 2C_{inj}}$ can be decomposed into two equivalent impedances, as shown in Figure 3.8, whose expressions are:

$$Z_A \triangleq \frac{Z_{inj}}{1 - G(s)} = \frac{1}{s \cdot 2C_{inj} \cdot (1 - G(s))} \ ; \tag{3.3}$$

$$Z_B \triangleq \frac{Z_{inj}}{1 - 1/G(s)} = \frac{1}{s \cdot 2C_{inj} \cdot (1 - 1/G(s))} \ . \tag{3.4}$$

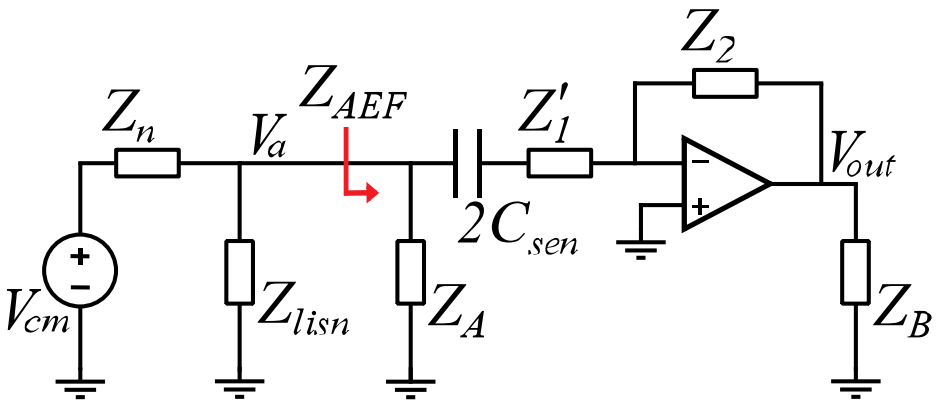

Figure 3.8: AEF equivalent circuit applying Miller's theorem.

Finally, looking at the circuit in Figure 3.8, the actual input impedance of the active filter Z_{AEF} is given by the parallel combination of Z_A and Z_1.

In conclusion, looking at the results, it becomes evident that the value of the injection capacitance over frequency can be shaped just properly defining the frequency response of the inner amplifier.

3.2.3 Filter design

As discussed in the previous section, the behavior of the AEF is totally determined by the characteristics of the amplifier. Therefore, in this section, the requirements for this element are defined. Then, a proper circuit is identified and verified. Finally, the complete AEF operation is also evaluated.

Looking at the expression of Z_A previously computed, it can be noticed that, in order to obtain the desired effect, *i.e.* to enhance the injection capacitance just in the conducted disturbances frequency range, this amplifier should present an high-pass type frequency response.
Another constraint is related to the low frequency attenuation. Indeed, the high-pass filter should sufficiently attenuate the line frequency and its harmonics so that the output of the operational amplifier does not saturate. This is needed also to prevent the AEF from operating where it is not required (in terms of frequency). Considering the amplitude of the line voltage, at least 60dB of attenuation at 50Hz are necessary in order to ensure an adequate safety margin. Indeed, in this way:

$$V_{in,50Hz}^{pk} = \sqrt{2} \cdot 230V \simeq 324.3V \implies V_{out,50Hz}^{pk} = G\left(j2\pi(50Hz)\right) \cdot V_{in,50Hz}^{pk} \simeq 0.32V \tag{3.5}$$

On the other hand, the amplifier gain in the EMI frequency range should be maximized, in order to obtain the maximum boost in terms of capacitance. Moreover, the phase shift in this frequency range should be as close as possible to 180 degrees, since injecting a signal that is not perfectly in opposition of phase with the disturbance signal would not allow perfect cancellation, degrading the performance of the AEF. Other considerations regarding the stability of the circuit will be discussed later.

In order to achieve the features previously listed, a 2nd order high-pass filter is needed. The related schematic is presented in Figure 3.9. Here $C_s \triangleq 2C_{sen}$ for brevity.

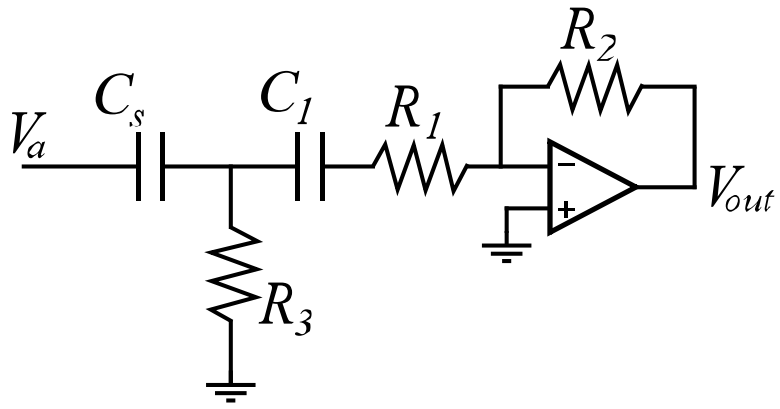

Figure 3.9: 2nd order high-pass filter employed in the AEF.

The associated transfer function has been computed as

$$G(s) \triangleq \frac{V_{out}}{V_a} = \frac{s^2 R_3 R_2 C_1 C_s}{s^2 R_3 R_1 C_1 C_s + s[R_1 C_1 + R_3(C_1 + C_s)] + 1} =$$

$$= \frac{R_2}{R_1} \cdot \frac{s^2}{s^2 + s\left(\frac{1}{R_3 C_s} + \frac{C_1 + C_s}{R_1 C_1 C_s}\right) + \frac{1}{R_1 R_3 C_1 C_s}} \ , \tag{3.6}$$

which, as expected, shows two zeroes in the origin, two poles (whose expression is cumbersome) and a mid-band gain given by the ratio between R_2 and R_1.

This expression shows 5 variables (the value of the 5 components) and 3 constraints (the two poles and the gain). This means that 2 degrees of freedom can be arbitrarily fixed.
Therefore, assuming $R1 = R3 \triangleq R$ and $C_s = C_1 \triangleq C$, the above expression simplifies as

$$G(s) = \frac{s^2 R_2 R C^2}{s^2 R^2 C^2 + 3sRC + 1} = \frac{R_2}{R} \cdot \frac{s^2}{s^2 + \frac{3}{RC}s + \frac{1}{R^2 C^2}} \ , \tag{3.7}$$

which shows two poles located at

$$p_1 \simeq 0.382 \frac{1}{RC} \qquad and \qquad p_2 \simeq 2.618 \frac{1}{RC} \ . \tag{3.8}$$

Considering a mid-band gain of almost 30dB and a required attenuation of -60dB@50Hz, using the graphical method it results that the two poles should be placed respectively at $3380Hz$ and $22.85kHz$. Therefore, by arbitrarily choosing $C = 2nF$, it follows that $R = 10k\Omega$.
Finally, the value of R_2 can be quickly derived by looking at the relation:

$$\text{when } \omega \gg p_2: \ |G(j\omega)| \approx \frac{R_2}{R} \stackrel{!}{=} 32 \implies R_2 = 32R = 320k\Omega. \tag{3.9}$$

At this point, the values obtained have been slightly revised in order to facilitate the choice of future additional elements, moreover, commercial values have been selected:

$$C_s = 2nF, \ C_1 = 3.3nF, \ R_1 = 3.3k\Omega, \ R_2 = 100k\Omega, \ R_3 = 6.8k\Omega. \tag{3.10}$$

This new set of values does not significantly change the characteristics of the filter. Repeating the computations we get:

$$|G(j2\pi 50)| = -67.1dB, \ p_1 = 2\pi(3.7kHz), \ p_2 = 2\pi(46.8kHz), \ \frac{R_2}{R_1} = 30.3\ . \tag{3.11}$$

To obtain the complete transfer function of the filter, the analysis should be repeated including the *real gain* of the operational amplifier. For this purpose an analysis by loop inspection has been done. By deriving the loop gain of this amplifier we can also check the stability of the circuit.

The considered operational amplifier is an $SGM8302$, that is characterized by:

- $100MHz$ unity-gain bandwidth
- $60MHz$ gain-bandwidth product
- $100mA$ output current
- Unity gain stability
- $155V/\mu s$ slew rate
- Rail-to-rail output

- Suitable and designed for video applications

Note that this device does not show high-end features (as well as the cost!), but it is just sufficient for our requirements, in order to keep it affordable for commercial applications.
Unfortunately, information about the precise open loop gain, as well as on the open loop output impedance behavior, are not available.
Therefore, considering a low-frequency gain of about 100dB, the first pole was assumed to be at a frequency of $\omega_{OA} = 2\pi(600Hz)$. No information are available regarding the second pole (except unity-gain stability), hence it has been ignored (even if this represents a best-case scenario).
Concerning the output impedance, a value of 10Ω has been supposed, as this is the value which best fits calculations and simulations with the practical results, as will be demonstrated later.

To analyze this structure, the circuit in Figure 3.10 might be considered (that is just the circuit in Figure 3.8 drawn in a more explicit way).
Here, some considerations should be done:

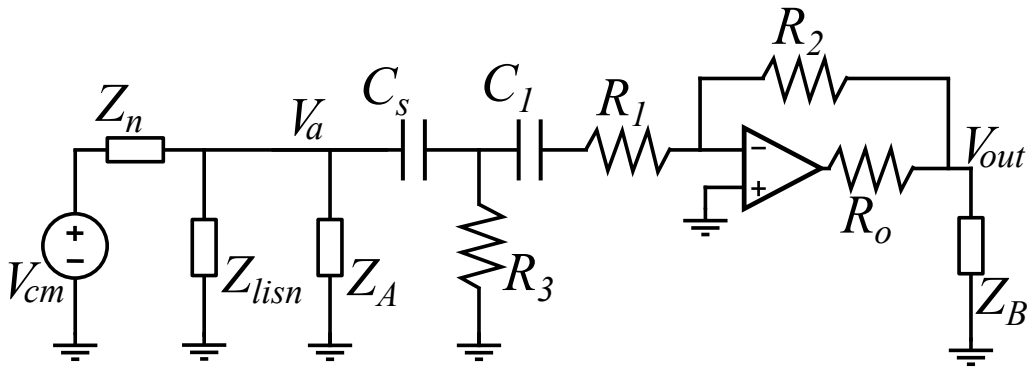

Figure 3.10: Miller's equivalent circuit, complete structure.

- As already said at the beginning of section 3.2.2, Z_{lisn} and Z_n represent the common mode impedances seen before and after the point where the AEF is introduced. Regarding Z_{lisn}, its impedance is well defined by standards and it can be considered approximately constant around 25Ω (except for very low frequencies). Conversely, the precise behavior of the CM noise source impedance

Z_n is very complicated to obtain (although some techniques have been proposed in [28][24]). Given the nature of this impedance (and also as done in most publications), a purely capacitive behavior has been considered. To estimate the value of this element, the stray capacitance between the switching node and protection earth has been measured, which was found to be 350pF.

- Still looking at Figure 3.8, it can be observed that the external loop causes a capacitive loading at the output of the OpAmp. This capacitor, combined with the output impedance of the OpAmp, introduces a phase delay that could endanger the inner loop stability. Therefore, the loop analysis should be conducted also considering the output impedance of the operational amplifier.

- The considered circuit includes also the Miller's impedances Z_A and Z_B, whose behavior is defined by (3.3) and (3.4). In those equations the precise gain of the high pass filter $G(s)$ (considering R_o) is needed, which can't be computed exploiting the loop gain, as it is still unknown. For this reason, an alternative way to derive this transfer function is required.

Hence, the first step in the circuit analysis is to derive the gain $G(s) \triangleq \frac{V_{out}}{V_a}$.
As mentioned, the usual method based on the loop gain can't be applied, thus an analysis based on delta-star transformation has been considered.
In fact, by looking at figure 3.11, a triangle structure made of Z_1, Z_2 and Z_{inj} can be recognized. Therefore, it can be replaced with the corresponding equivalent star

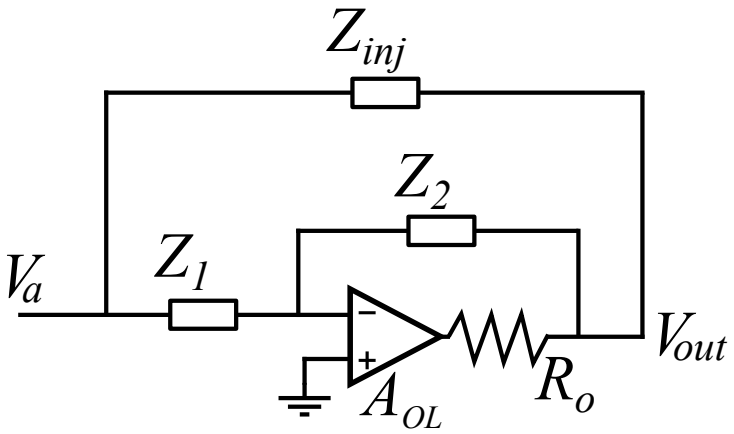

Figure 3.11: High pass filter with the external loop.

representation, as done in Figure 3.12, where:

$$Z_1^s = \frac{Z_{inj} \cdot Z_1}{Z_1 + Z_2 + Z_{inj}},\ Z_2^s = \frac{Z_2 \cdot Z_{inj}}{Z_1 + Z_2 + Z_{inj}},\ Z_3^s = \frac{Z_1 \cdot Z_2}{Z_1 + Z_2 + Z_{inj}}\ . \tag{3.12}$$

Now the circuit can be solved. The usual solving method is slightly complicated by

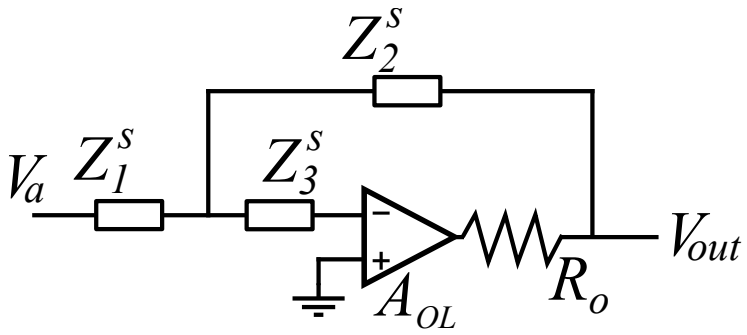

Figure 3.12: Circuit of Figure 3.11 using the equivalent star representation.

the fact that a real amplifier, with limited GBP and non-zero output impedance, is considered. The block diagram associated to this circuit has been derived and shown in Figure 3.13, where:

$$\alpha = \frac{Z_2^s + R_o}{Z_1^s + Z_2^s + R_o}\ , \qquad \beta = \frac{Z_1^s}{Z_1^s + Z_2^s + R_o}\ ,$$
$$\gamma = \frac{Z_1^s + Z_2^s}{Z_1^s + Z_2^s + R_o}\ , \qquad \delta = \frac{R_o}{Z_1^s + Z_2^s + R_o}\ . \tag{3.13}$$

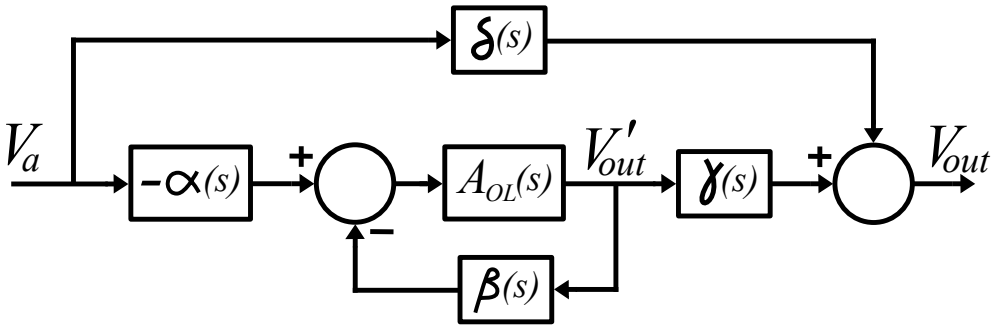

Figure 3.13: Block diagram according to loop inspection including R_o.

Therefore, the gain of this circuit can be computed as:

$$G(s) \triangleq \frac{V_{out}}{V_a} = \delta - \alpha \cdot \frac{A_{OL}}{1 + \beta A_{OL}} \cdot \delta\ . \tag{3.14}$$

The above transfer function has been computed using MATLAB and the results are shown in Figure 3.14. For comparison, also the results obtained simulating the circuit with LTspice (superimposed to the Matlab traces) and those using (3.7) are reported in this figure. This allows to appreciate the effect of neglecting the output impedance of the OpAmp.

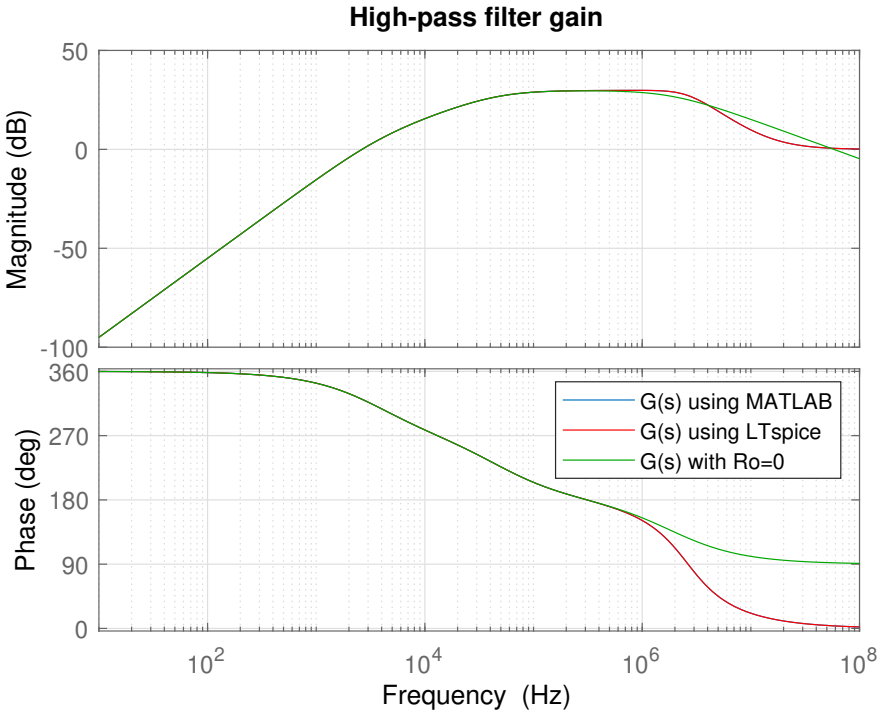

Figure 3.14: Bode plots of the inner high pass filter $G(s)$ computed using MATLAB, simulated with LTspice (superimposed on the previous one) and using (3.7).

At this point, the Miller's impedances, *i.e.* the effective impedance at the input side and the loading effect on the internal filter of the external loop, can be computed exploiting (3.3) and (3.4).
In Figure 3.15 and 3.16 the calculated results have been shown, as well as the simulated ones. Again, in both cases, the two traces are superimposed.

Finally, the actual loop gain can be derived. Looking at the schematic of Figure 3.10, it results:

$$T'_{in}(s) = A_{OL}(s) \cdot \frac{Z_T}{Z_T + R_2} \cdot \frac{(Z_T + R_2)//Z_B}{(Z_T + R_2)//Z_B + R_o} \ , \tag{3.15}$$

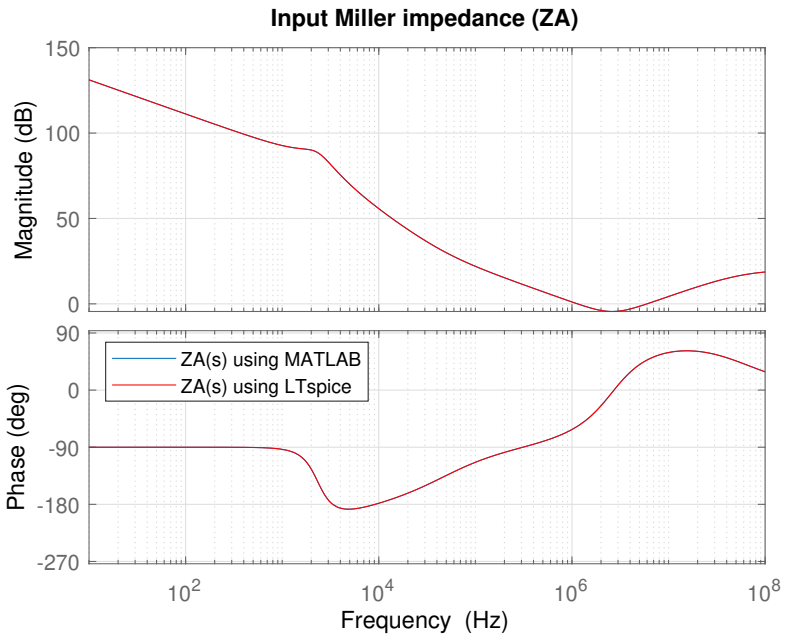

Figure 3.15: Bode plots of the input Miller's impedance Z_A, computed with MATLAB and simulated with LTspice (superimposed).

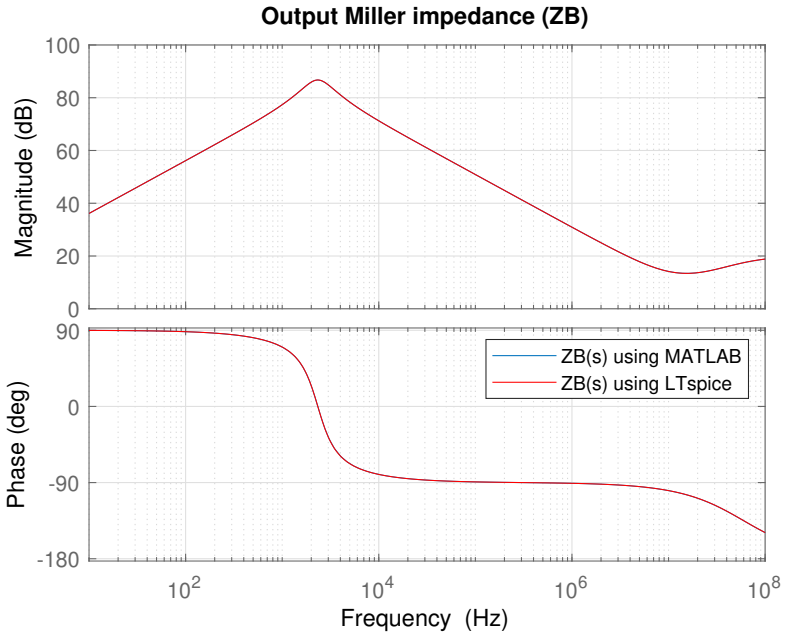

Figure 3.16: Bode plots of the effective high-pass filter load impedance Z_B, computed with MATLAB and simulated with LTspice (superimposed).

where: $Z_T = (Z_n//Z_{lisn}//Z_A + Z_{Cs})//R_3 + Z_{C1} + R_1$.

Its Bode plots are presented in Figure 3.17. Here, transfer functions have probably become too complex for MATLAB and it could not find a solution. Therefore, just LTspice results (obtained with Middlebrook method [19]) have been considered. For comparison, the plots under ideal conditions are also shown. It is now

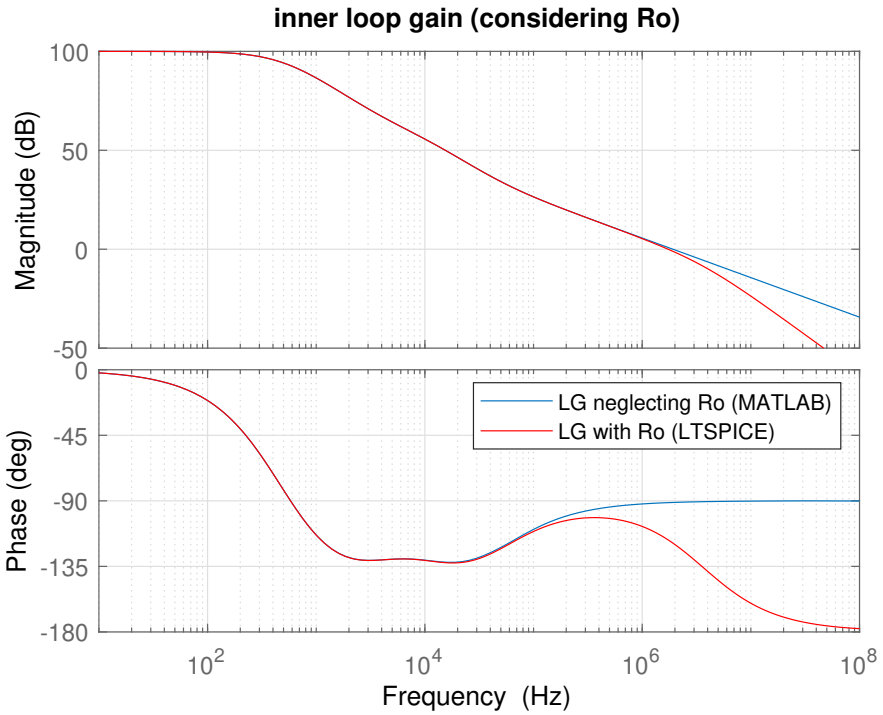

Figure 3.17: Bode plots of the inner loop gain, considering or not the output resistance of the OpAmp.

evident that the presence of the output resistance of the OpAmp and of the loading impedance introduces a pole close to the crossover frequency, which degrades the phase margin. Fortunately, the circuit still shows an acceptable phase margin of 63.2 degrees.

This fact can be exploited to roughly estimate the output impedance of the OpAmp, which, remember, was not specified on the datasheet by the manufacturer.
To enhance this effect a circuit made of the high-pass filter and a $47nF$ load capacitor has been considered.

The step response measured on a practical circuit is shown in Figure 3.18. Con-

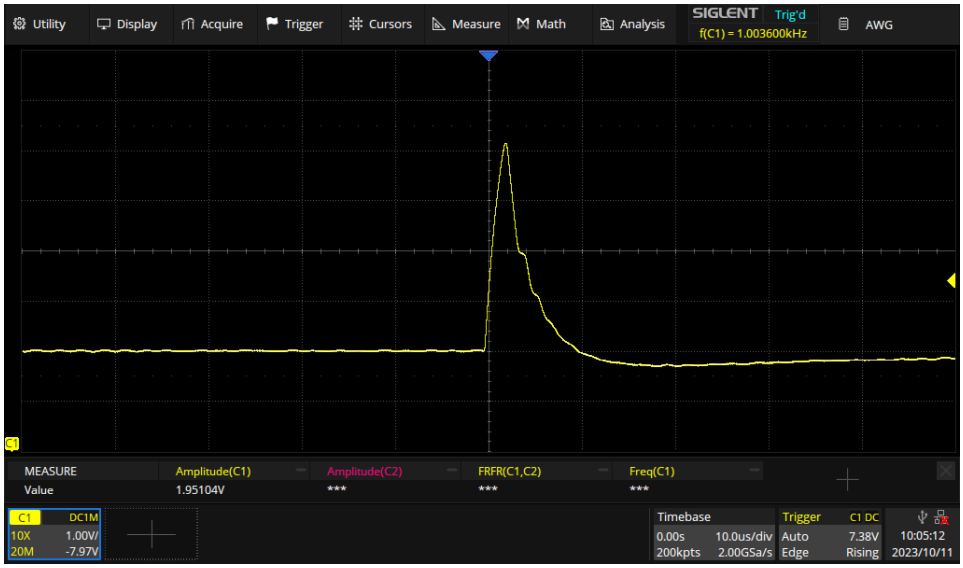

Figure 3.18: Step response of the practical circuit.

versely, in Figure 3.19, the simulated step response considering 3 different output resistances is presented. As can been seen, the simulation which best fits the ex-

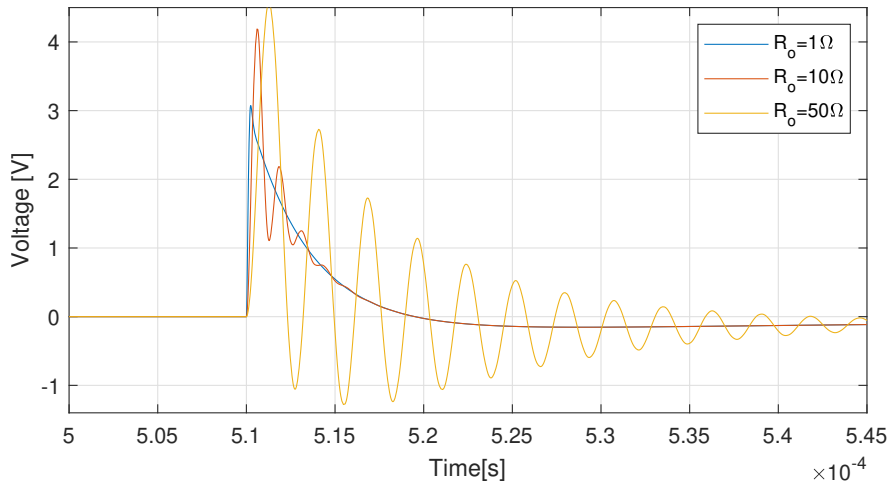

Figure 3.19: Step response of the simulated circuit, considering $R_o = 1\Omega$, $R_o = 10\Omega$ and $R_o = 50\Omega$.

perimental results is the 10Ω one; therefore, this value has been taken into account for all calculations.

At this point, the external loop can be analyzed.
To do that, the inner amplifier can be represented with its equivalent unidirectional two port model, as shown in Figure 3.20, where:

$$Z_{in} = (Z_{C1} + R_1)//R3 + Z_{Cs} \ , \qquad Z_{out} \approx \frac{R_o}{1 + T'_{in}(s)} \ , \tag{3.16}$$

and the gain G(s) is as already shown in Figure 3.14.

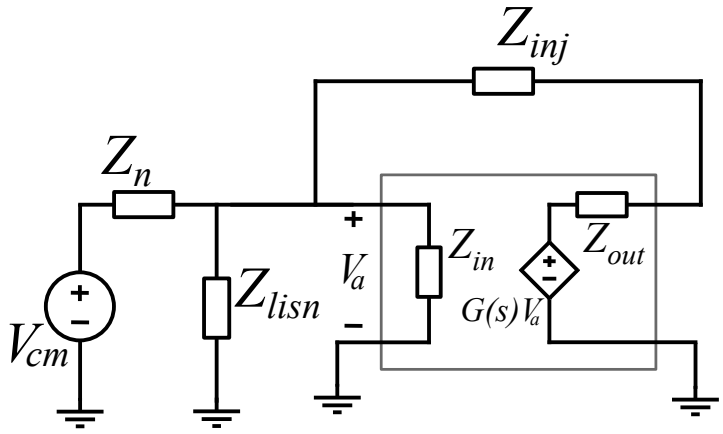

Figure 3.20: AEF circuit for external loop evaluation.

Now the external loop gain can be computed:

$$T_{ext} = G(s) \cdot \beta_{ext} \qquad with : \beta_{ext} = \frac{Z_n//Z_{lisn}//Z_{in}}{Z_n//Z_{lisn}//Z_{in} + Z_{inj} + Z_{out}} \tag{3.17}$$

Unfortunately, MATLAB did not show reliable calculations and the actual loop gain has been directly derived from simulation applying, again, Middlebrook's method. Hence, the structure of Figure 3.21 has been arranged and, by means of (3.18), the external loop gain has been derived, whose bode plots are shown in Figure 3.22.

$$T_{ext} = \frac{T_v T_i - 1}{T_v + T_i + 2} \ , \tag{3.18}$$

where T_v is the ratio between the voltages before and after the voltage test generator V_t (namely, the voltages at nodes X and Y) and, similarly, T_i is the ratio between the currents flowing before and after the current test generator I_t (namely, the currents flowing through the measure $0V$ generators V_{m1} and V_{m2}.

Given this plot, the stability of the external loop can be evaluated. Two phase margin can be recognized considering the two 0dB axis crossing of the loop gain

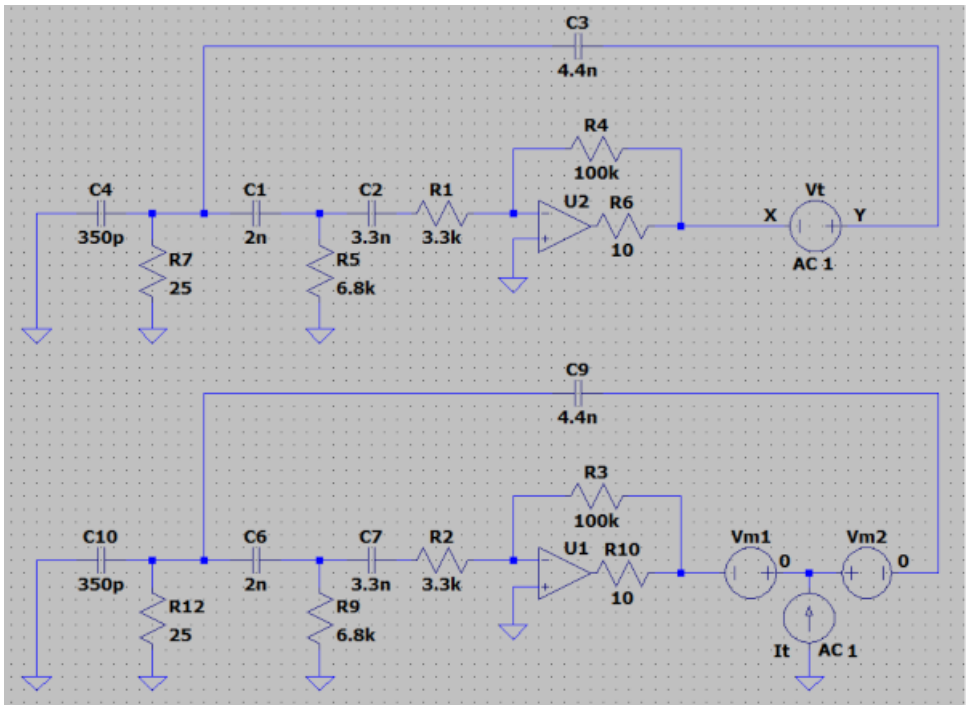

Figure 3.21: AEF simulation circuit for external loop gain derivation by means of Middlebrook's method.

magnitude plot. For this circuit, 54 degrees and 93 degrees has been obtained for the low frequency and high frequency phase margin respectively, measured as shown in Figure 3.22. Hence, looking at these results, no stability issues should arise for this circuit.

Unfortunately, as already mentioned and for the reasons already discussed, it is not easy to precisely define the impedances involved in the system, both because the source impedance has a complicated nature and because, at these frequencies, the effect of the parasitic elements becomes decisive. In addition, there is also a lot of uncertainty about the OpAmp parameters. Hence, the analysis just performed is not really aimed at precisely establishing the final circuit, but rather at investigating its operation and understanding the purpose and effect of the various elements, so that it is known where to act in case the circuit does not behave in the intended manner.

To this purpose, additional elements have been introduced in the diagram in

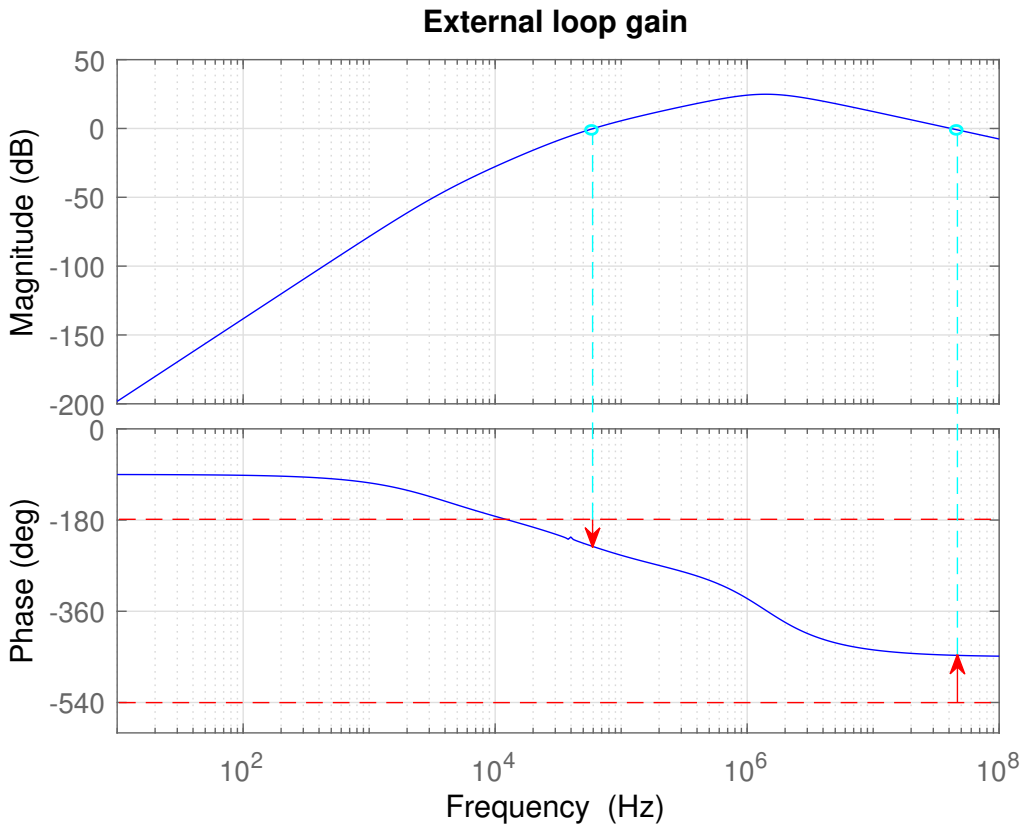

Figure 3.22: External loop gain Bode plots.

Figure 3.23, which have a negative impact on the overall performance of the filter, but also allow to solve possible oscillations that could arise due to imperfect modelling of the system. Specifically, the capacitor C_2 limits the high frequency gain of the inner amplifier, improving its stability and sensitivity to high frequency noise, while the resistor R_4 introduces a resistive component on the equivalent impedance of the AEF, which enhances its damping. The improvement in terms of phase margin of the external loop can be seen considering the parametric simulations of Figure 3.24. The value of these components will be determined in the experimental phase, depending on the need.

At this point, a final comment about the actual advantages of this active EMI filter can be made.
As already said, the idea behind this structure is to enhance the capacitance of a couple of $2.2nF$ Y-capacitors that is actually mounted and taken as a reference.

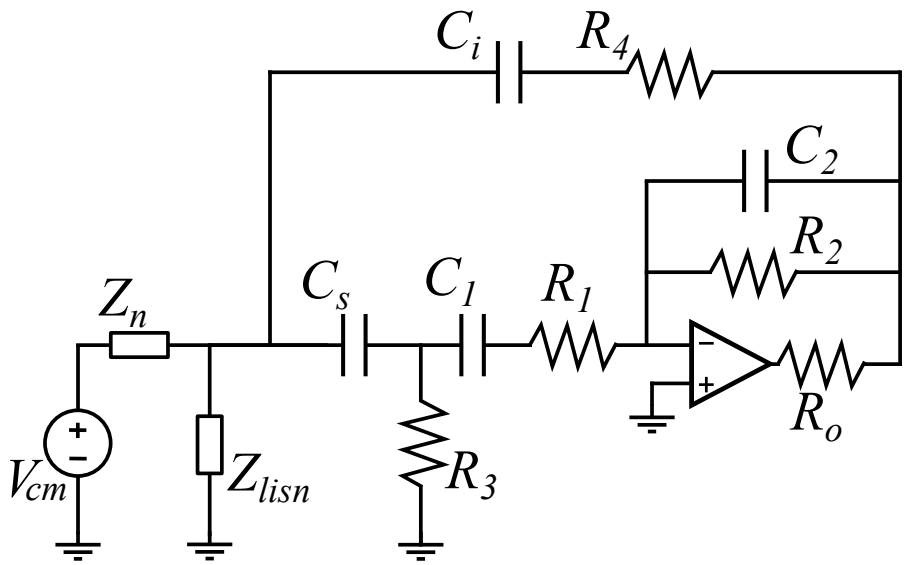

Figure 3.23: AEF schematic with additional elements (R_4 and C_2) for improving stability.

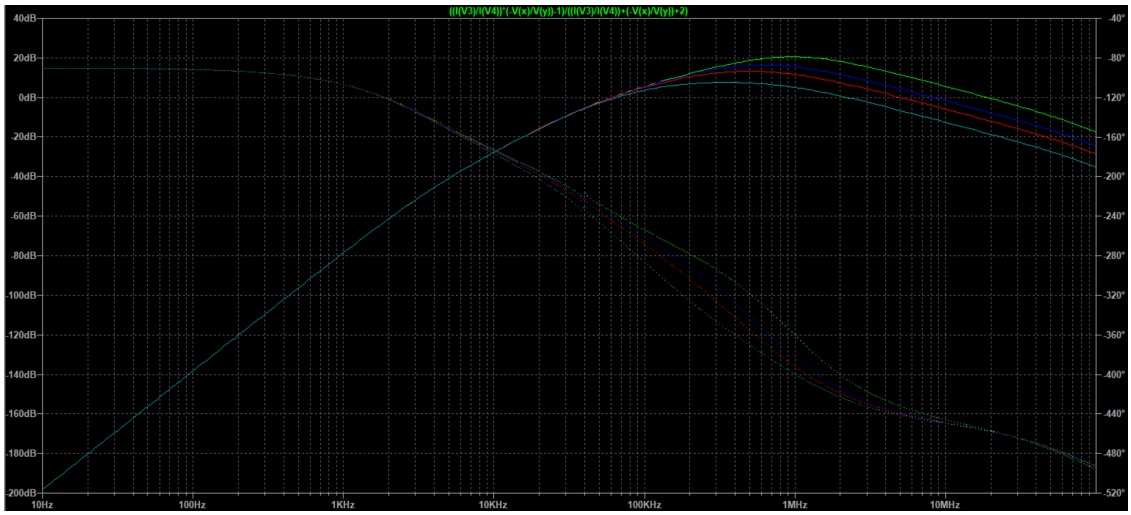

Figure 3.24: External loop gain parametric simulations, sweeping the value of R_4 from 10Ω to 200Ω (10Ω green, 50Ω blue, 100Ω red, 200Ω cyan).

Therefore, for a fair comparison, the injection capacitors of the AEF have been sized in the same way *i.e.* $C_i = 4.4nF$. The input impedance shown by this structure can be easily derived by looking at the circuit of Figure 3.10:

$$Z_{AEF} = Z_A // Z_{in} = \frac{Z_{inj}}{1 - G(s)} // (Z_{C1} + R_1) // R3 + Z_{Cs} \ . \tag{3.19}$$

In Figure 3.25 the magnitude of this input impedance is presented, compared with those of a $4.4nF$ capacitor and also those of a $140nF$ capacitor. From this compar-

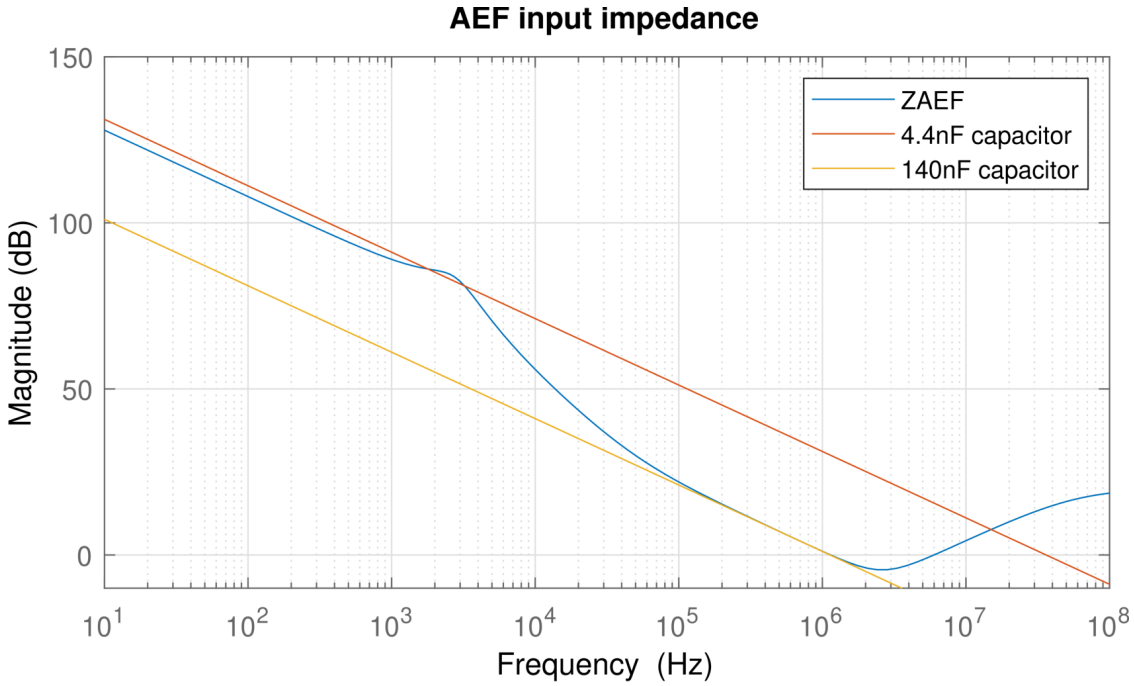

Figure 3.25: Comparison between the magnitude of the input impedance of the AEF Z_{AEF}, those of a $4.4nF$ capacitor and those of a $140nF$ one.

ison it can be recognized that at low frequency (and especially at line frequency) the AEF behaves almost like a $4.4nF$ capacitor, *i.e.* it doesn't affect the injection impedance. Therefore, if the passive circuit is designed to be compliant with leakage currents regulations, it will also be compliant considering the active circuit. As the frequency increases, the active part enhance the injection impedance. As can be seen, in the conducted emissions frequency range the AEF reaches the impedance of a $140nF$ capacitor, *i.e.* 32 times larger. Then, after a certain frequency, its impedance degrades and it is no longer reliable for disturbances suppression. This means that other passive elements should be introduced to cover this frequency range, which, however, would be relatively small in sizes, considered the frequency.

In Figure 3.26 a comparison between a $2.2nF$ capacitor (employed in the AEF) and a $22nF$ capacitor is presented, in order to highlight the advantages in terms of size reduction of the active solution. Note that a common mode filter is built

using two of these capacitor. Note also that the expected theoretical improvement computed above is much larger than that considered in this comparison. Both capacitors are $400V_{AC}$ rated and Y2 safety rated, as they should withstand line voltage.

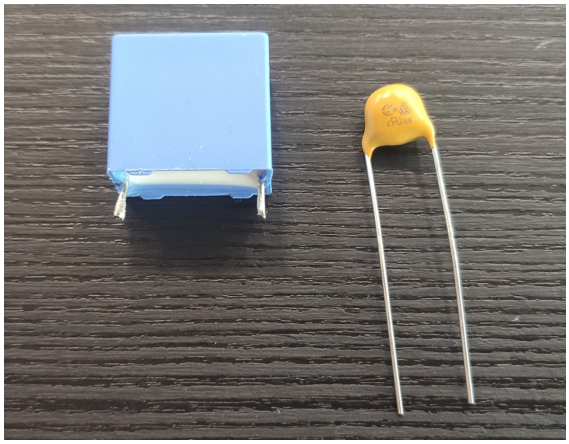

Figure 3.26: Comparison between the size of a $2.2nF$ capacitor used in the active filter and a $22nF$ capacitor potentially employed in an equivalent passive filter.

3.2.4 Simulations and practical implementation

Once completed the analysis and design phase, in order to evaluate in advance the operation of the circuit in a practical case, some simulations has been conducted. Then, the final considered structure has been implemented on a PCB and its performance has been evaluated in different real scenarios. In this section, this last phase is described.

To verify the performance of the designed circuit in terms of EMI reduction, some LTspice simulations have been arranged. Of course, these results are not representative of the practical results that will be obtained on the real circuit, firstly because the considered DUT are different, but also because the model is missing many elements that affect the results (like parasitics, other external disturbances, non idealities, etc...). However, this analysis gives an idea of the actual capabilities and potential of the AEF solution.
Thus, the model of a generic flyback DC-DC converter has been considered. This

model is based on a *LT1241* integrated circuit and passive components also includes some non idealities. This last point is very important in an EMI simulation, in order to obtain realistic results. Particularly, the $350pF$ stray capacitor between the switching node and protection earth, considered up to now, has been included. Finally, the Active EMI Filter and the model of a LISN has been introduced to properly evaluate the emissions. Given this circuit, also reported in Figure 3.27, a time domain analysis has been performed.

Then, the line and neutral LISN output signals are probed and, using mathemat-

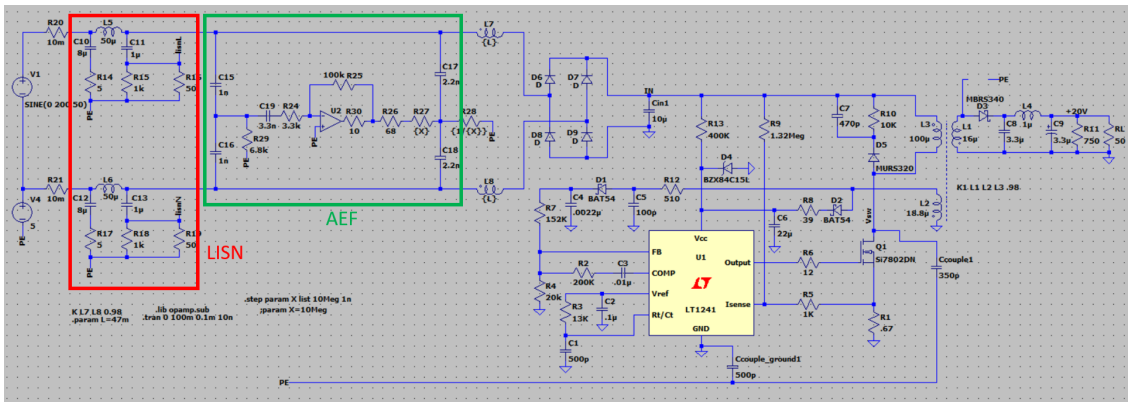

Figure 3.27: The simulated circuit includes the flyback model, the main stray components, the Active EMI Filter and the LISN.

ical operators, the common mode signal is extracted. Considering its FFT (Figure 3.28), the results obtained with the AEF can be compared with those using a simple pair of capacitors, in order to understand the contribution of the active circuit.

These results are coherent with those expected. In fact, at low frequency (*i.e.* between $150kHz$ and $2MHz$) the AEF shows an improvement in terms of noise reduction of up to 20dB compared with the passive solution. Then, beyond $2MHz$, its performance starts to degrade.

Before implementing the circuit in a PCB, a provisional prototype has been arranged (showed in Figure 3.29), in order to evaluate its behavior, to check the stability and to refine the value of certain components. The results of circuit characterization will be shown in Section 3.3.2.

During this phase, some unexpected instabilities arose when the prototype was connected to the final circuit. The solution to this problem was found by observing

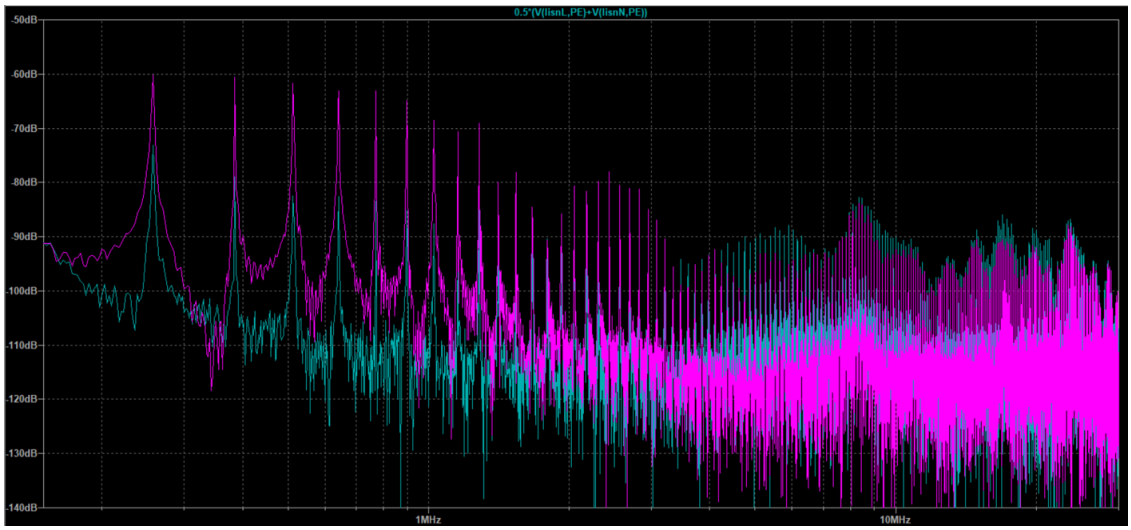

Figure 3.28: Simulated CM conducted emissions using the designed AEF (blue) and using an equivalent passive capacitor ($2.2nF$+$2.2nF$) (purple).

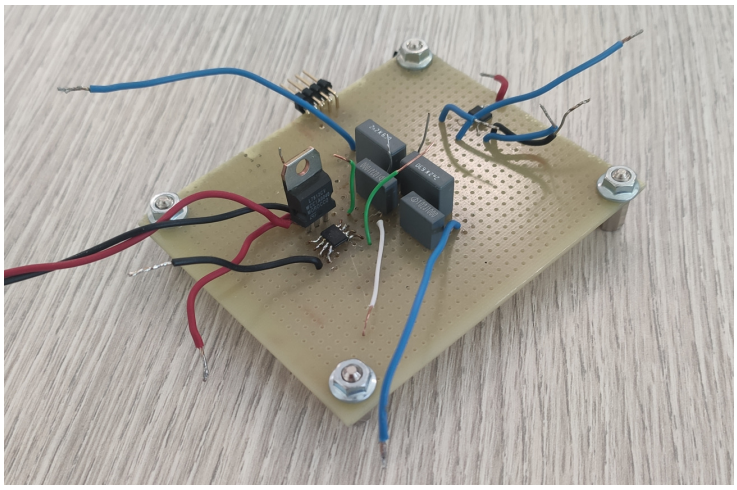

Figure 3.29: Prototype of the AEF, mounted on a breadboard, for preliminary tests.

that the power for the AEF was supplied using an auxiliary power supply present on the DUT board. However, since this supply was also used for other parts of the circuit (such as the communication and control sections) it was very disturbed and that was probably sufficient to destabilize the active filter. In fact, by powering the circuit with an external laboratory generator, this problem did not arise anymore. Therefore, in the design of the board, special attention was paid to the

power supply section of the operational amplifier, introducing a DC-DC isolated power supply (which galvanically separates the supplies), a π filter for differential mode noise, and an LC filter for common mode, both before and after the power supply, as illustrated in the final circuit in Figure 3.30.
In addition, to achieve stability, a 68Ω resistance in series to C_i was needed.

The final schematic of the circuit is shown in Figure 3.30. Then, the PCB shown

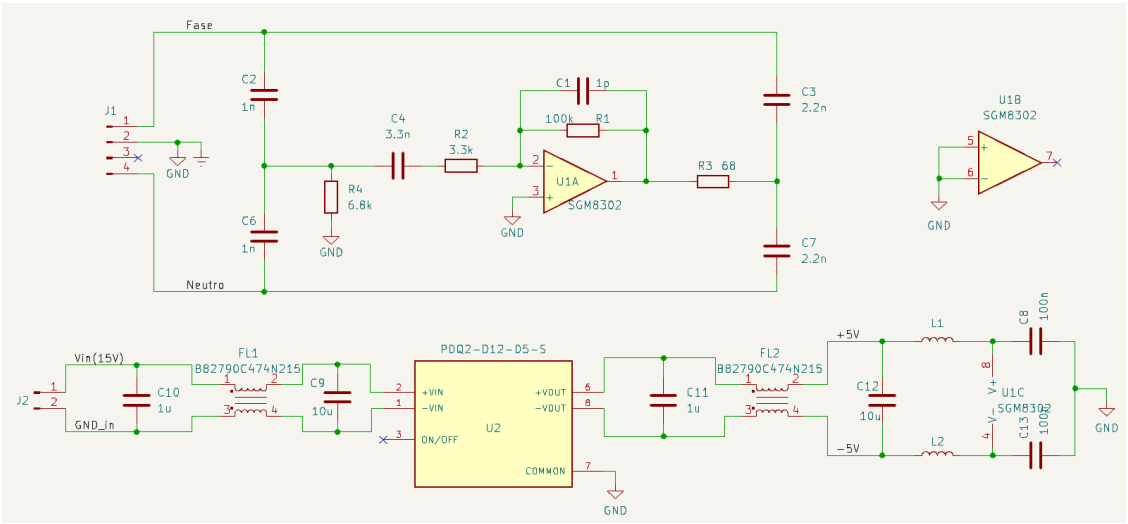

Figure 3.30: Schematic of the final circuit.

in Figure 3.31(a) has been designed. Here, particular attention was paid to separate the various sections (AC section, sensing section, output section, supply section, "noisy" supply section) to avoid possible unwanted coupling. For the same reason, the ground plane on the second layer has been removed under the AC section, as well as under the output region. Moreover, the reference before and after the isolated DC-DC supply has been kept separated; therefore, as can be seen, each region has been covered with the respective ground plane.
In Figure 3.31(b) a preview of the final circuit is shown. The board is 4,5cm x 4,5cm large. As can be seen (also looking at Figure 3.32), almost one third of the board is occupied by the DC-DC converter and the CM-chokes. This section can certainly be made smaller, however, in this prototype, we wanted to make sure it didn't interfere with the operation of the AEF. Also the mounting holes and the connectors take up a lot of space and the actual area that this circuit would occupy once integrated in the DUT would be almost half of that currently occupied.

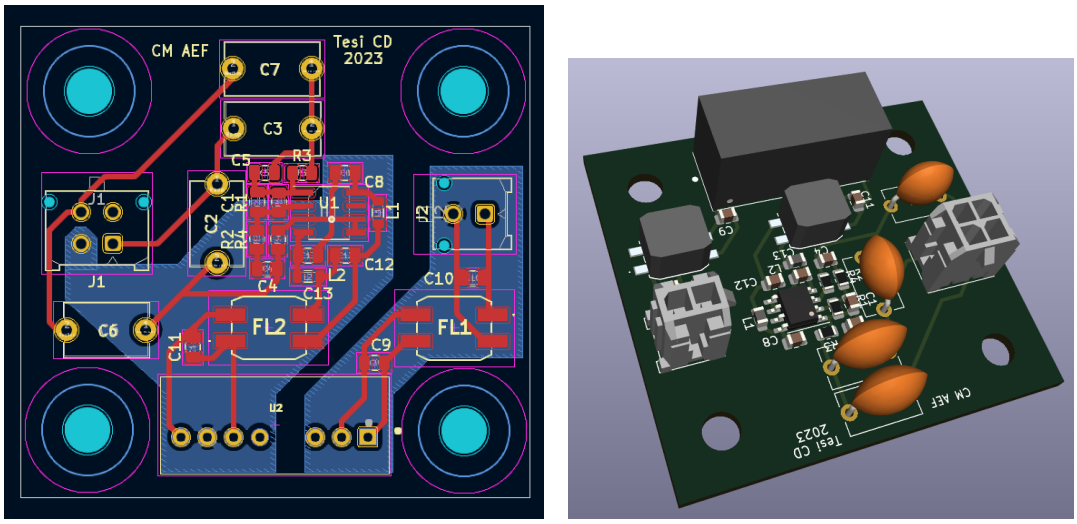

(a) (b)

Figure 3.31: (a) PCB layout and (b) 3D preview of the final circuit.

Finally, the circuit has been assembled on the designed PCB and its picture is showed in Figure 3.32.

The results obtained from practical applications of this circuit will be shown later in Section 3.3.2.

3.3 Integrated Active EMI Filter

During the first phase of exploration and information collection, the possibility of using an *integrated* AEF has been considered. Integrated circuits, compared to discrete solutions, have the advantages of minimizing parasitics and, simultaneously, of eliminating the variability due to component placement. This means that they allows to achieve the most repeatable results. Moreover, they also consent to minimize the size, including most of the passive network inside the chip. In addition, the integrated amplifier architecture can be optimized for this application, instead of using a general purpose OpAmp.
Conversely, as the circuit is designed without knowing the actual device where it will be introduced, it is reasonable to suppose that performance optimization has

Figure 3.32: Photo of the final circuit.

been sacrificed in favor of versatility. However, the main problem with this solution is related to the fact that apparently this technology is not so popular among IC manufacturers. In fact, at the moment, only *one* component is commercially available, that is the *TPSF12C3-Q1* by Texas Instruments (in turn, available from January 2023). This poses serious limitations related to potential problems of component availability.
For the reasons just described, both the integrated and the discrete solutions have been considered, analyzed and compared.

In this section, the analysis of the considered integrated AEF, as well as the comparison with the discrete homemade one (described in Section 3.2) and its performance in practical cases are presented.

3.3.1 Integrated AEF analysis

As previously said, currently, there is only one integrated AEF commercially available: the *TPSF12C3-Q1*.
This component is specifically designed to implement a common mode filter. The employed topology is the voltage sensing - current compensation one. This means that a filter made with this integrated circuit would behave similarly to the home-made discrete one, as they share the same base structure. Hence, they are perfectly comparable.
Inside the very compact SOT-23 14 pin package, the IC includes the amplifier and most of the surrounding networks. Externally we have to place just the sensing and injecting capacitors and part of the compensation network. Looking at the block diagram of Figure 3.33, it can be noticed that the component presents 4 inputs, as it is intended to be implemented in a 3-phase system with neutral. However, in this case, we are considering a single-phase system, so the excess inputs were grounded[1]. Then, the sensed signals pass through a conditioning network, which includes a line frequency filter, that removes this unwanted component, and a summation, that extracts the common mode component. Afterwards, the CM signal is high pass filtered, inverted and amplified by an active stage, whose compensation can be externally refined. Then, Texas Instruments suggests to introduce an additional external compensation network in order to improve the overall stability and avoid resonances. Finally, the processed signal is injected back using a single capacitor on the neutral. The generation of a CM signal relies on the presence of X-capacitors between the two (or four) phases, which can be considered short circuits for EMI frequencies. This asymmetric solution has been discarded during the discrete AEF design, as non idealities or the absence of X-capacitors close to the injection point can cause an unbalanced injection of the compensation signal, which translates in DM and CM noise *generation*.
Inside the IC it is provided also thermal protection, ESD protection and an internal reference voltage used to shift the amplifier reference and provide both positive and negative compensation with a unipolar supply.

[1]Note: due to the lack of information I am not sure that this is the ideal method to exploit this circuit in a single-phase system. However, by looking at the datasheet, it can be seen that if the circuit is used in a three-phase system without neutral it is indicated to connect the unused input to earth. Therefore, in this case, it was decided to act in a similar way.

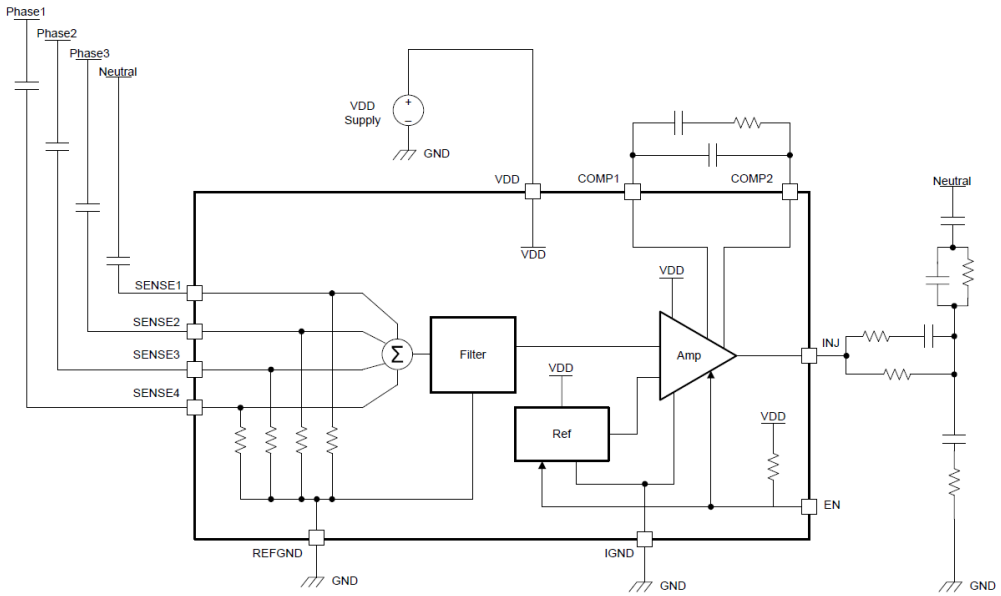

Figure 3.33: Internal block diagram of the IC by Texas Instruments [13].

The big problem that has limited the use, analysis and study of this component is the lack of available information. In fact, on the datasheet there is only a generic description of the behavior of the circuit, similar to the one just made, but not much is said about its precise internal structure. For the sizing of external components, broad values are suggested, to be modified through trials and errors until the desired result is achieved. Alternatively, a spreadsheet is provided, which returns the proposed values based on the introduced system parameters. This approach is poorly suited for a deep analysis and limits the usability.

Beside this, the associated evaluation board has been considered (Figure 3.34). This device simply implements on a PCB the circuit suggested in the datasheet, except for the sensing and injection capacitors. The inputs and outputs are provided on a practical pin-strip connector.

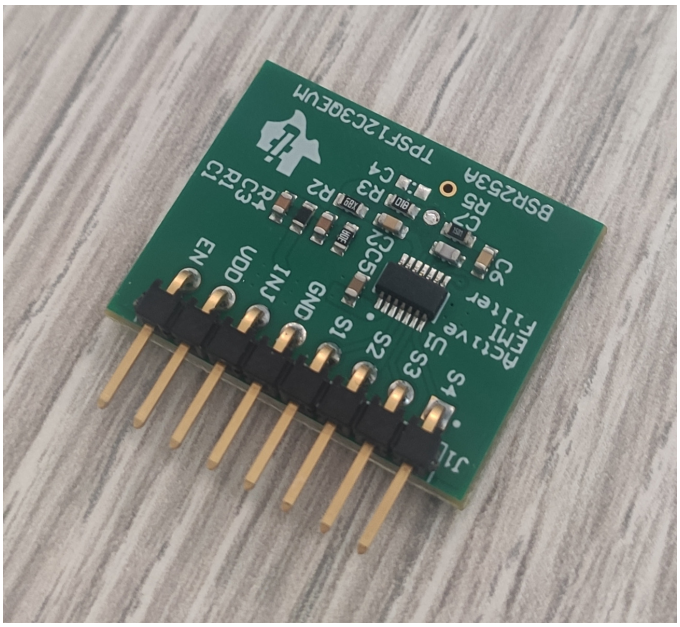

Figure 3.34: *TPSF12C3-Q1* Evaluation Board.

3.3.2 Practical verification, experimental testing and comparison with the discrete AEF

Once the integrated circuit structure and its operation have been comprehended, some practical verifications can be carried out in order to better understand how this circuit works and how much differs from the home made one. These two circuits result well comparable, as they employ the same topology (fully capacitive, VSCC) and they use similar injection capacitance value ($4.7nF$ for the integrated AEF, $2.2nF + 2.2nF$ for the discrete one).

Firstly, the magnitude of transfer function $G(s)$, defined, in this case, as the ratio between the voltage at the output of the amplifier (before the external compensation network) and the voltage applied at the sensing capacitors, has been evaluated. The same quantity has been experimentally evaluated also for the homemade AEF.
In Figure 3.35 a comparison between the calculated and the measured behaviors of the homemade AEF is shown. As can be seen, the experimental results follows quite well the simulated ones.
On the other hand, in Figure 3.36, a comparison between the IC transfer function and the discrete AEF one is presented. Here it can be observed that the IC behaves

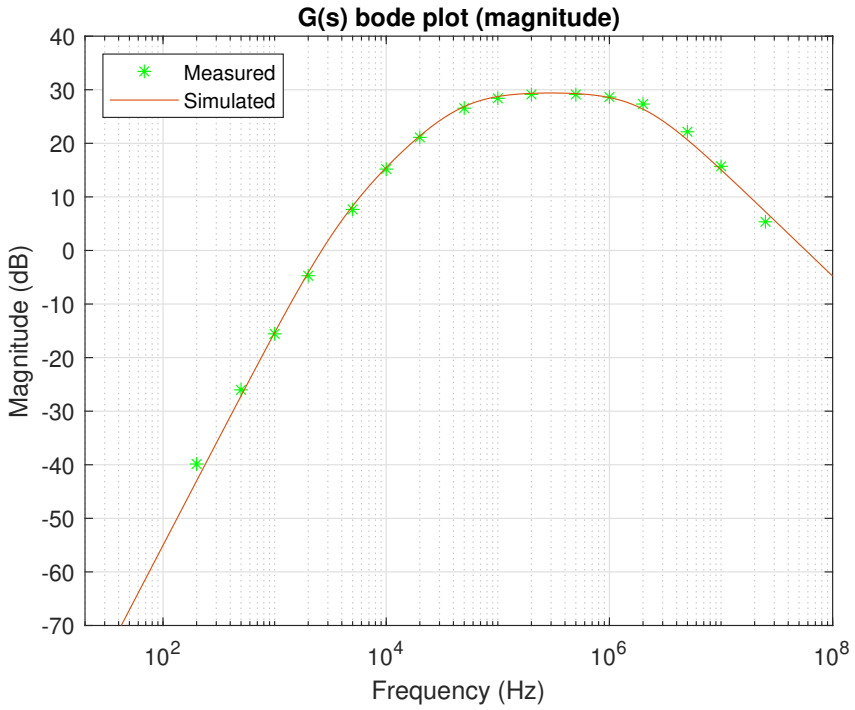

Figure 3.35: Comparison between the simulated $G(s)$ of the *discrete* AEF and the experimentally evaluated one.

very similarly to the discrete filter, except for a constant gain. In fact it shows a second order high-pass filter behavior, with two zeroes in the origin, one pole located around $7kHz$ and two poles at $40kHz$.

Then, the common mode signal suppression capabilities of the two circuits has been evaluated. To do that, the same signal has been applied on both the inputs of the AEFs by means of an RF signal generator. Then, the signal has been observed at the node between the 50Ω internal impedance of the generator and the AEF inputs (Figure 3.37(a)). In a certain way, we are looking at the output of an RC low pass filter, so we expect to get a response of that kind.

As can be seen from simulations in Figure 3.37(b), at low frequency the AEF shows a very high impedance, so a very low current flows through the 50Ω impedance and the voltage drop is negligible. Beyond $100kHz$ the impedance of the AEF is lower than 50Ω and the effect of the EMI filter becomes appreciable. Around $700kHz$ the voltage at this node reaches the minimum and then it begins rising, as the AEF starts losing its effect. Note that the simulated output has been shifted up by $6dB$, in order to make this plot comparable with the measured ones. Indeed,

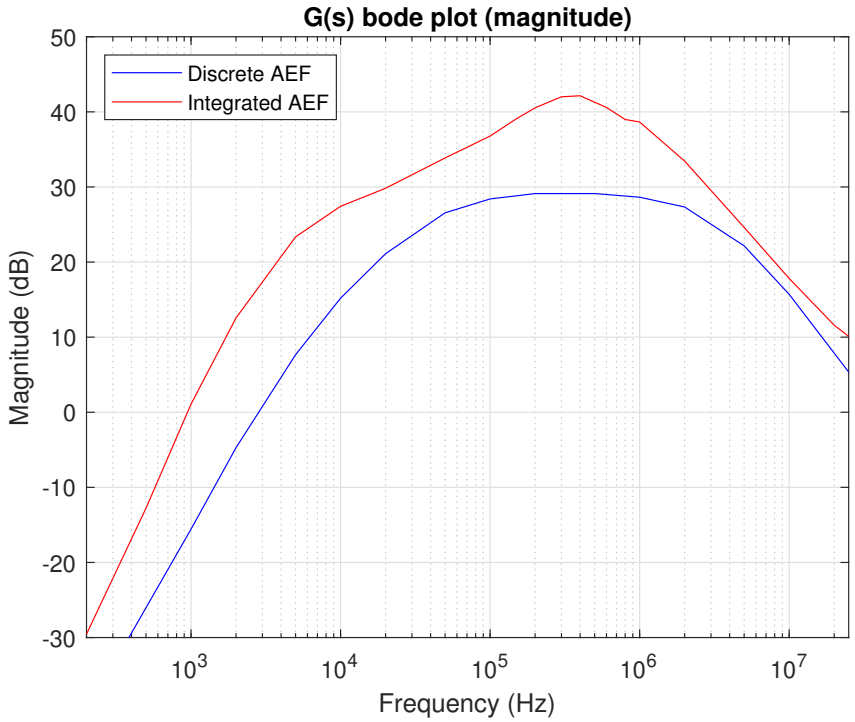

Figure 3.36: Comparison between the $G(s)$ experimentally evaluated in the discrete AEF and in the integrated one.

the instrument employed for practical evaluations (the R&S ESRP) automatically compensates the 1/2 factor given by the 50Ω impedances.
Looking at the experimental results of the discrete AEF (Figure 3.38(a)) it can be observed that it follows quite well the simulation. Repeating the same analysis also on the integrated AEF (Figure 3.38(b)) we can recognize that it shows very similar behavior to the discrete one, except above $10MHz$, where the integrated solution behaves slightly better (sign of better management of parasitic components, probably).

At this point, the experimental setup of Figure 3.39 has been arranged, in order to evaluate the actual performance of the circuits.
The device under test is the auxiliary power supply section of a photovoltaic grid-connected inverter. This is implemented with a flyback converter, which is controlled in a sophisticated way in order to achieve specific requirements. For instance, switching frequency depends on the operating point and includes a small frequency jitter to reduce EMI emissions.

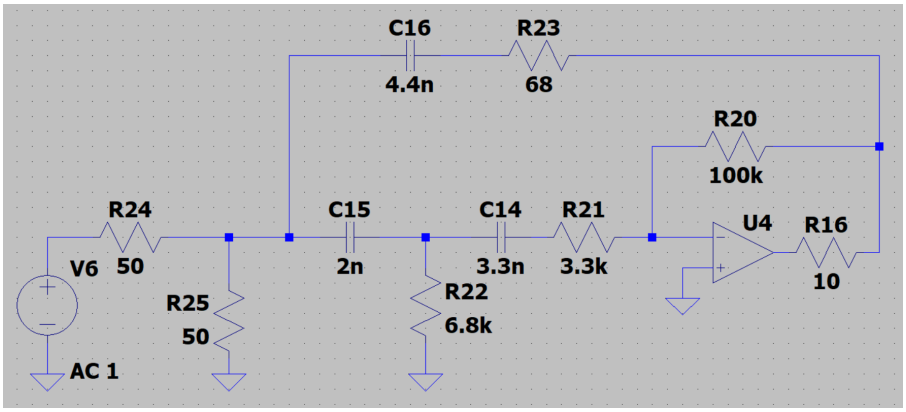

(a)

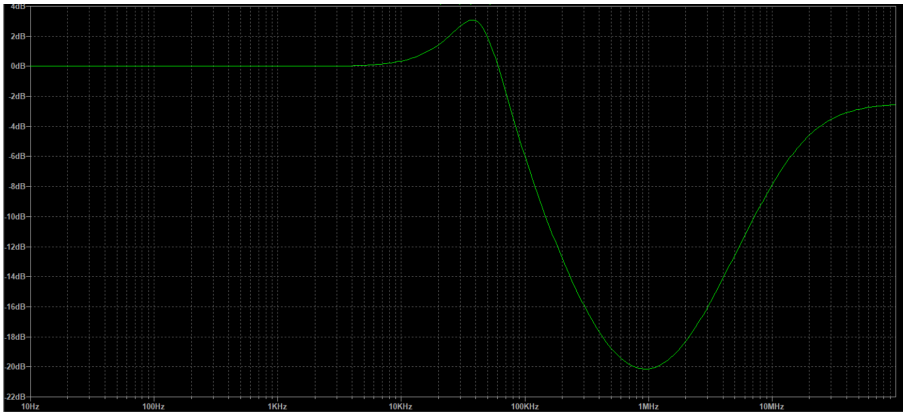

(b)

Figure 3.37: AEF input impedance evaluation: (a) the simulated circuit; (b) the simulation output (voltage on R_{25} shifted by 6dB).

The EMI filter under analysis has been positioned in correspondence of the DUT supply connectors. The filters have been connected by means of cables directly soldered on the flyback board. At the other end a Micro-Fit connector has been installed, in order to quickly switch between the different filters or allow rapid adjustments. As can be seen, the supply for the filter is taken from the board and, more specifically, using one of the voltage outputs generated by the flyback converter itself.

Then, still looking at Figure 3.39, between the DUT and the grid is located the LISN, which extracts the conducted emissions generated by the converter and filtered by the EMI filter. Afterwards, the output of the LISN is passed through the homemade DM/CM splitter (which will be described in detail in Chapter 4) that

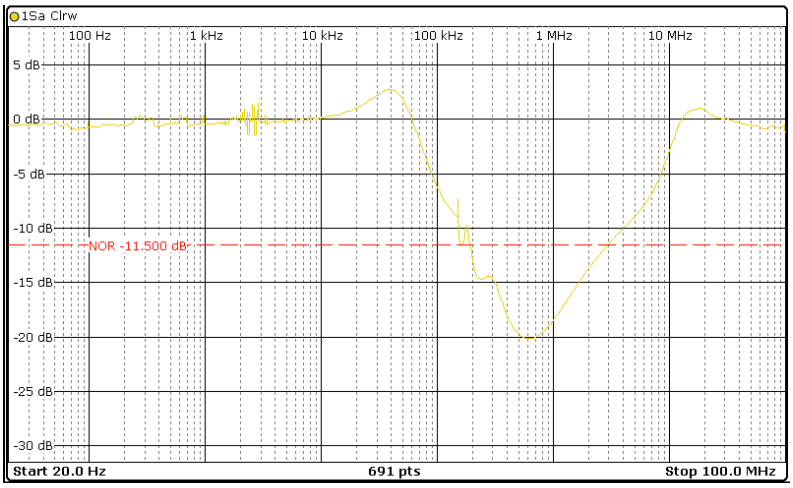

(a)

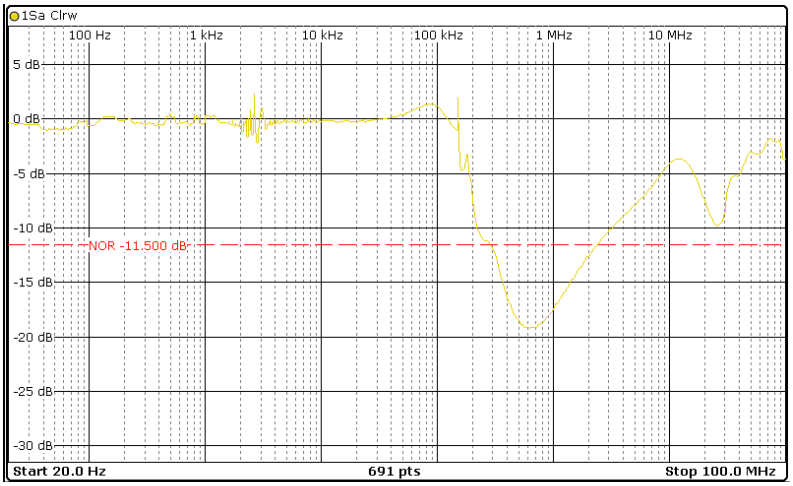

(b)

Figure 3.38: AEF input impedance evaluation: (a) the practical measurement on the discrete AEF; (b) the practical measurement on the integrated AEF;

extracts the CM component of the disturbances. Finally, the CM signal is delivered to the EMC spectrum analyzer, where it can be visualized.

This setup does not strictly comply with the directives for a proper compliance analysis (for instance regarding cable length and positioning, device positioning, external environment, etc...), however it is sufficiently refined to allow to obtain meaningful and reliable results, close to those obtainable with a full-compliance test.

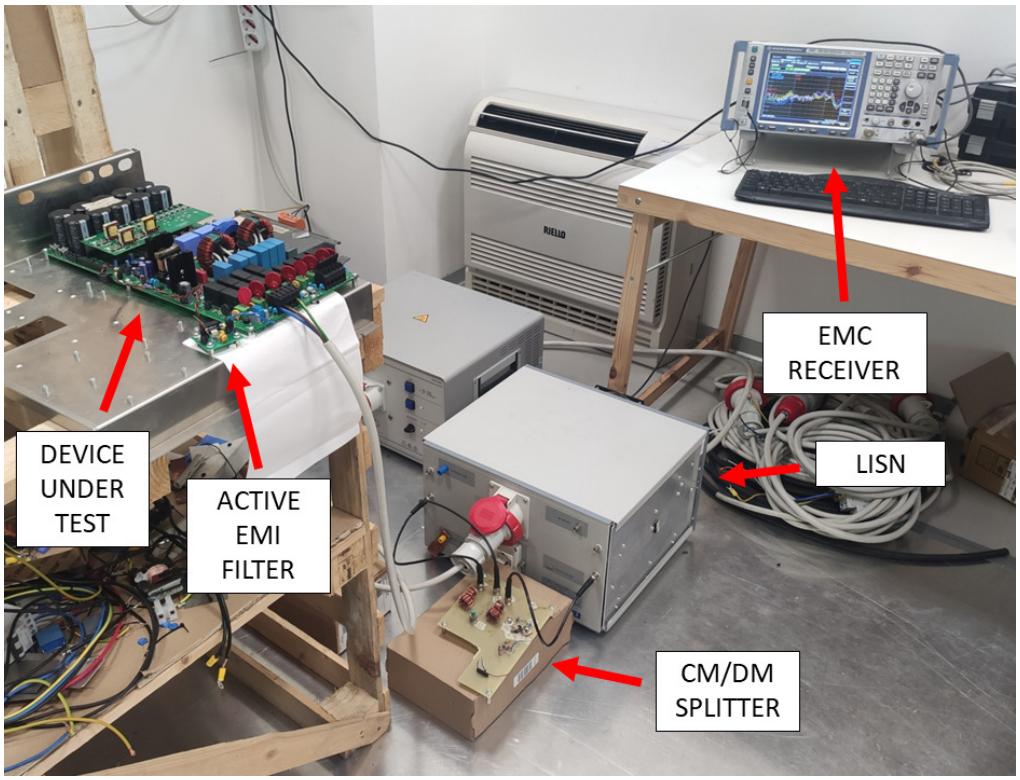

Figure 3.39: Photo of the experimental setup for AEF evaluation and comparison.

Before checking the results, the proper operation of the discrete AEF has been verified. First, the voltage signal at the output of the operational amplifier has been observed. Looking at Figure 3.40 it can be noticed that it does not present noticeable oscillations at specific dominant frequencies. In addition, the signal amplitude does not cause saturation.

Then, the output current of the OpAmp has been checked, in order to identify possible current saturation phenomena. In Figure 3.41 a differential measurement of the voltage drop on the 68Ω resistor of Figure 3.41 is shown. As can be seen, this voltage does not go beyond $400mV$, therefore the correspondent peak current is $6mA$, well below the maximum output current of the OpAmp of $100mA$.
The same verifications have also been done on the integrated AEF, which did not present any problems.

Finally, the performance in terms of actual noise reduction improvement has

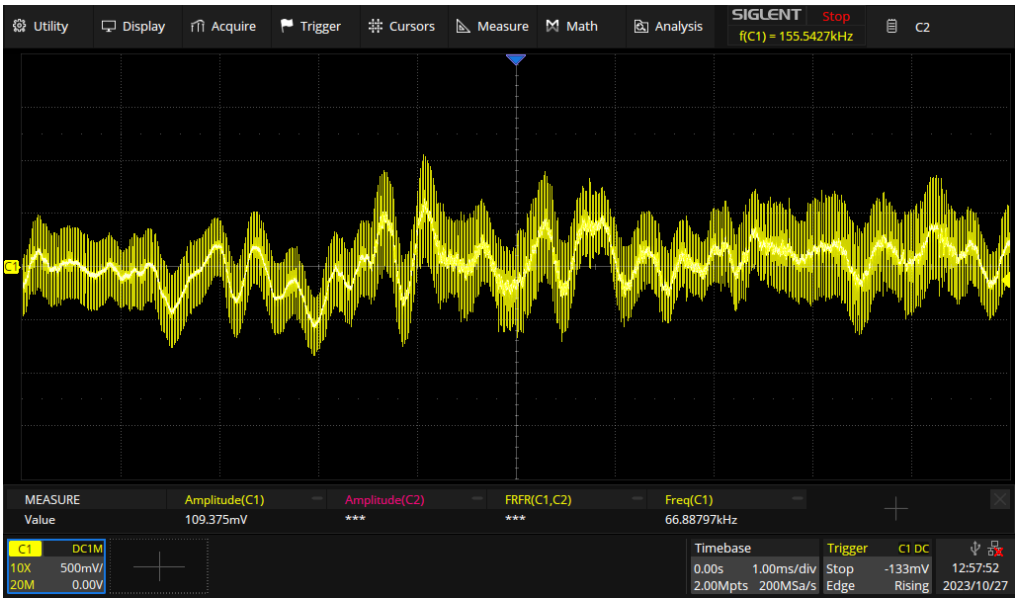

Figure 3.40: Output signal of the OpAmp in the discrete AEF.

Figure 3.41: Voltage drop on the 68Ω resistance in series with the injection capacitor in the discrete AEF.

been observed. To give a reference, the emissions level using a purely passive solution (made of two $2.2nF + 2.2nF$ capacitors connected in place of the AEF) has been recorded.

At first, a comparison between this passive solution and the discrete AEF has been done, in order to evaluate the actual increase in performance generated by the active part. The results are shown in Figure 3.42. Only the traces obtained us-

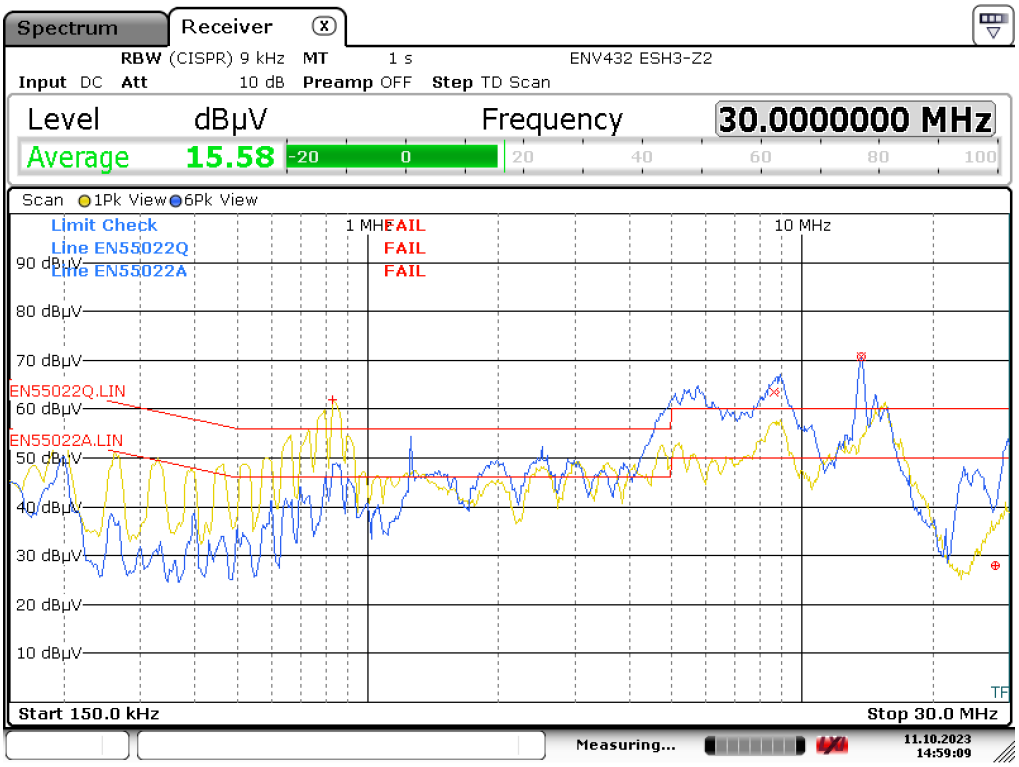

Figure 3.42: Common Mode conducted emissions of the inverter's power supply, employing: in yellow the purely passive solution based on a pair of $2.2nF$ capacitors, in blue the homemade discrete AEF.

ing Max Peak detector are presented, in order to keep the image neat, clean and readable. Average detector measurements showed very similar results and wouldn't add any information for the comparison, so they have not be included. Quasi-peak measurements have not been considered here.

Looking at the figure, the results are very consistent with those expected. In fact, the AEF largely overtakes the performance of the passive capacitors in the first part of the EMI frequency range. The achieved improvement is between $10dB$ and $20dB$. As expected, above $1MHz$ the performance of the AEF starts decreasing, since at this frequency the amplifier loses its capabilities. In fact, up to $4MHz$ it almost equals the passive performance and after it behaves much worse. However, it must be taken into account that these results can be considered reliable up to

$10 - 20MHz$, due to CM/DM splitter limitations discussed in Chapter 4.

Afterwards, the performance of the integrated AEF has been evaluated. In Figure 3.43, the emissions of the DUT with the integrated AEF are shown, together with the discrete AEF and the passive ones.

As can be seen, the Texas Instruments filter manages to enhance the EMI reduc-

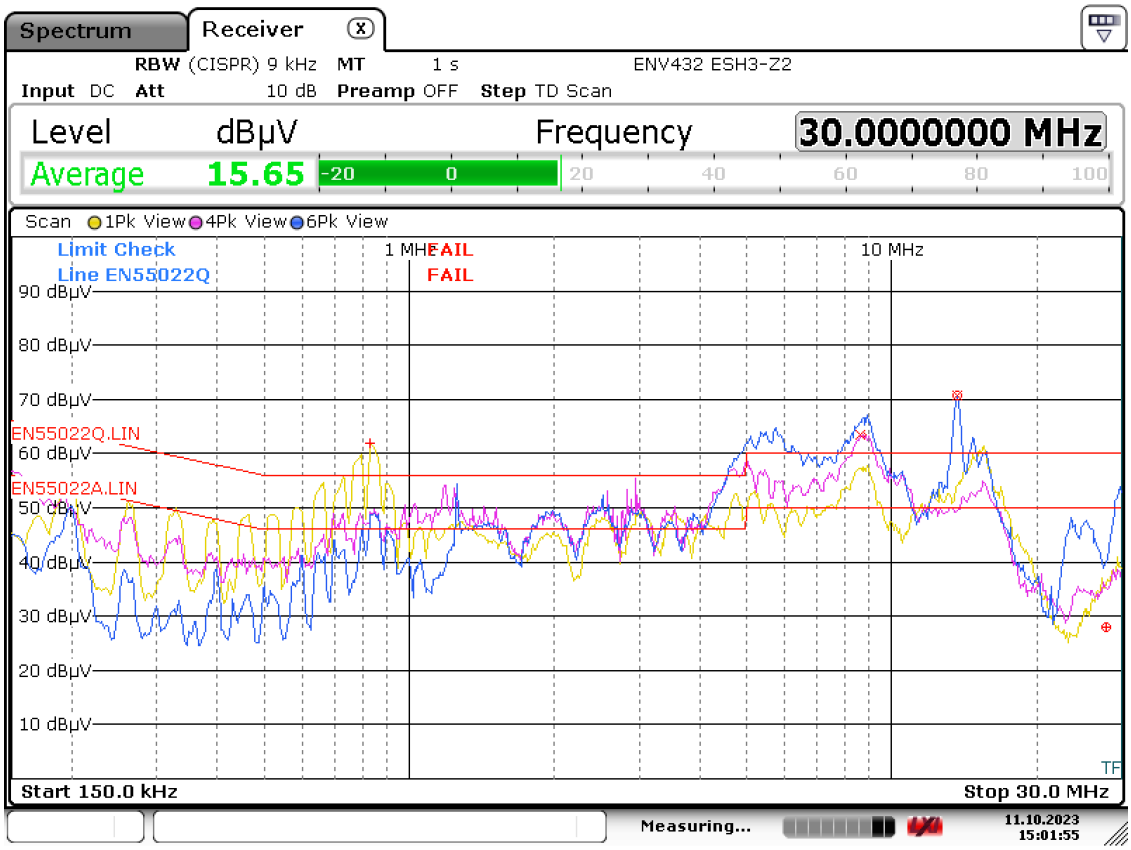

Figure 3.43: Common mode conducted emissions of the inverter's power supply employing 3 different filters: in yellow the reference trace using the purely passive solution, in blue the results using the discrete AEF and in purple the emissions using the Texas Instruments integrated AEF.

tion in the low EMI frequency range, although, in this case, the improvement is limited to $3 \div 10dB$. Above $1MHz$ (but also a little before) even in this case the performance of the AEF degrades.

Then, to confirm the results just obtained, the analysis have been repeated in

another DC-DC converter. Compared to the previous one, this is a much simpler system, with fixed switching frequency, without a metallic structure around it and without many other sections of the circuit that commutate and operate simultaneously with the main converter, generating additional noise. The results using the 3 different filters are shown in Figure 3.44.

In this case, the discrete AEF showed very good performance in a much larger

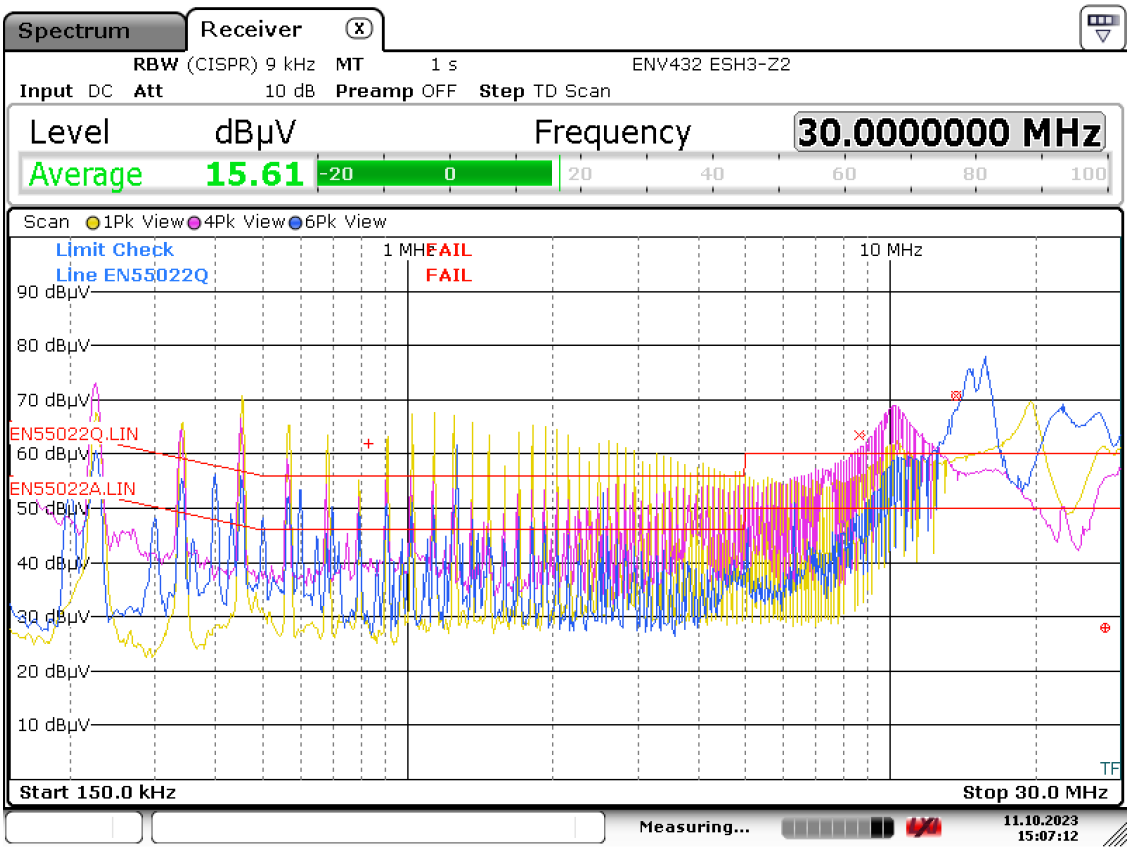

Figure 3.44: Common mode conducted emissions of the simple flyback converter employing the 3 filters: in yellow the purely passive solution, in blue the discrete AEF and in purple the integrated AEF.

frequency range, *i.e.* up to $10MHz$. Here the filter showed an improvement between $10dB$ and $20dB$ compared to the passive solution. Regarding the Texas AEF, again this filter managed to enhance the passive filter performance, but still does not reach the homemade AEF ones. Indeed, in this case the improvement is included between $2dB$ and $10dB$.

3.3.3 Final remarks, limits and further developments

Looking at the results of Figures 3.43 and 3.44, the effectiveness of the AEF solution has been demonstrated and, in those practical tests, the homemade discrete filter showed significantly better performance than the integrated one. Presumably, the Texas AEF would behave better in more complicated situations, where its more sophisticated compensation network would be required. In addition, no tests were conducted about the repeatability of the results, using various replications of the circuits.

It should be noticed that with an operational amplifier of acceptable cost it is possible to obtain more than acceptable results. To further extend the capabilities of the circuit, one could try to exploit amplifiers with improved characteristics. This is done in many papers (like [22, 16, 26]), however, looking at the practical verifications, it seems that much better results than those obtained in this work cannot be obtained anyway.
In other works other solutions have been proposed to try to further improve the AEF capabilities, for instance, in [6] a power stage is introduced in order to compensate for larger disturbances. In recent articles like [17, 8], the signal processing circuit has been implemented using a DSP. This last solution showed very good results, however, as pointed out in this work, the effort required to implement it and especially its flexibility must be evaluated and considered.

In the final phase of the development of this work, it has been tried to introduce this active filtering stage on the output stage of a photovoltaic inverter (which was the initial purpose of this work).
Thus, the two filters previously presented have been used to replace the Y-capacitor of the LCL common mode EMI filter at the output of the inverter.
Imagining obtaining a boost of performance similar to that described in the previous chapter, in this case the gain in terms of size-reduction would be huge. In fact, supposing to be able to get a 30 times larger simulated capacitor (like in Figure 3.25), this means that, to achieve the same attenuation, both the CM-inductors can be reduced by the same factor.
However, since these are inductors that must be able to handle the entire output current of the inverter (which can be in the order of a few tens of amperes), this

leads to an enormous reduction in occupied space, and the advantages grow as grows the current managed by the DUT. Figure 3.45 shows a comparison of the size of the original $1.1mH$ inductors mounted on the inverter and the same circuit but with $330\mu H$ inductors, that is just a reduction by a factor 3. Assuming we want to create a $45\mu H$ CM-choke, this would mean that the windings in the figure would be reduced to a single turn.

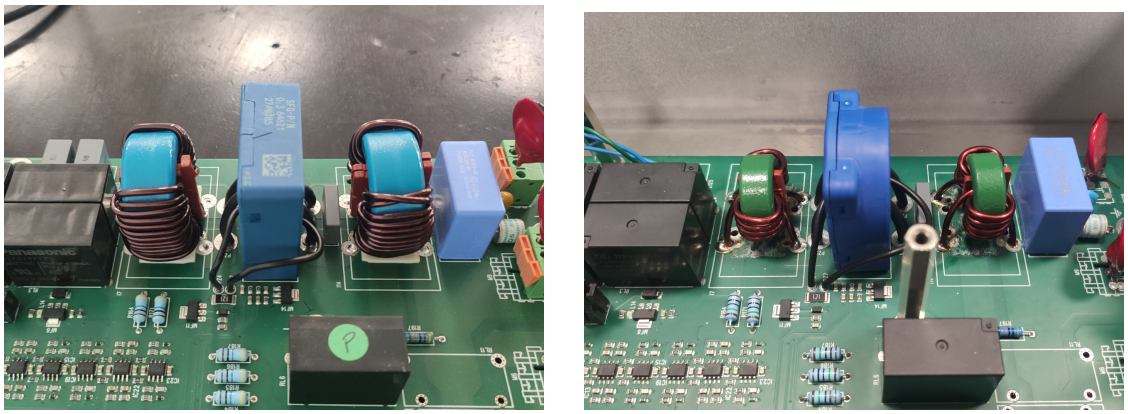

Figure 3.45: On the left the inverter with the original $1.1mH$ CM-chokes of the EMI filter. On the right the same board but with $330\mu H$ chokes installed.

A system like this is extremely more complex than the converters evaluated in the previous section, due to a series of reasons:

- First of all, there are multiple sources that contribute to conducted emissions (and not a single switching node), as a photovoltaic inverter is composed of many sections that perform different functions simultaneously;
- Then, the various passive EMI filtering elements and the various equivalent impedance of the different sections combine to form a network that is extremely complicated to model, mainly because all the parasitic elements should be carefully taken into account;
- In addition, during its operation, the circuit can pass through various states and operating conditions, which also involve the opening and closing of relays. This behavior modifies the network seen by the possible AEF.

All these aspects make the modeling of the noise source impedance very complex

and, especially, variable in time. Furthermore, this ultimate model should also take into account the variability due to tolerances and the positioning of the various components.
Therefore, the OpAmp compensation network must be sufficiently robust to guarantee its stability in all possible states of the inverter and also against the variability of the parameters.

Unfortunately, poor results have been obtained from the active EMI filters under analysis. Regarding the discrete AEF, it behaves well during certain transitory phases, but, when the system reaches steady-state, it starts oscillating at $70kHz$ (Figure 3.46), and, in certain situations, it even saturates. Obviously, in these conditions the OpAmp can't operate properly. On the other hand, the integrated AEF cannot achieve stability in any condition.

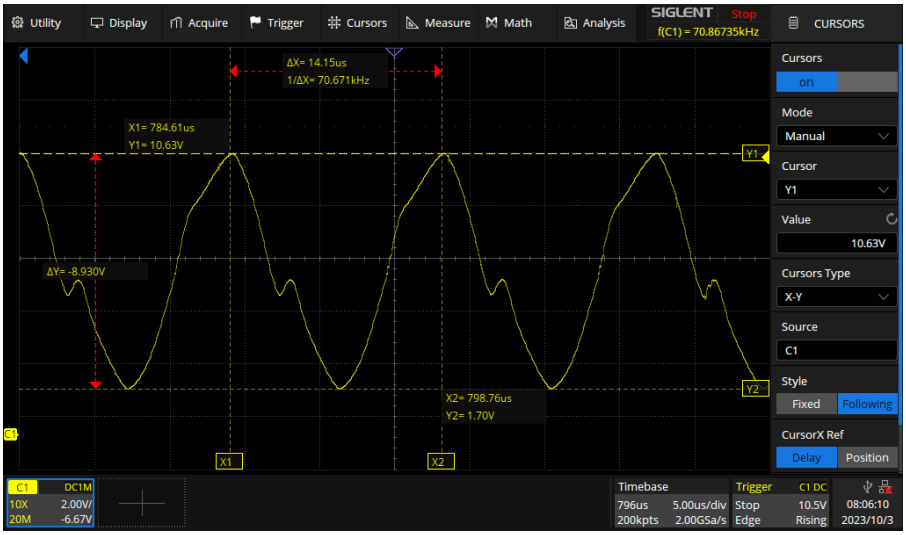

Figure 3.46: Oscillation at the output of the discrete AEF OpAmp when introduced in the inverter.

This final analysis highlighted one of the problems of these circuits *i.e.* versatility. In fact, each active filter must be designed specifically for the application in which it will end up and this requires a much greater effort than a passive filter. Hence, a more detailed analysis is surely needed to make this system operate properly.
It would even be interesting to investigate whether it is just possible to create such

a filter, capable of satisfying all these requests while maintaining acceptable performance. Unfortunately, there was not the chance to explore further, but next studies will be oriented on this topic, with the aim to achieve the described advantages.

Chapter 4

CM/DM splitter: design and characterization

In this chapter, the realization of a splitter device capable of extracting the DM and CM components from the noise signal will be described. This is an extremely useful tool in the EMI filter design phase. In fact, although the regulations evaluate emissions by looking at the overall signal present on each line, EMI filters, due to their structure, act separately on the common mode and differential mode components of the noise, as also widely shown in the previous chapters.
A tool like this allows to know the actual composition of the signal generated by the DUT and, in this way, it becomes possible to optimize and refine the sizing of the EMI filter, intervening specifically in the points where the filter will have the greatest effectiveness.

Despite its usefulness, not many devices of this type are commercially available and even fewer (if any) for three-phase systems. There is also a particular type of LISN called Delta-LISN which incorporates one of these systems within it and, consequently, offers the DM and CM signals directly on its outputs. However, also this system is not very widespread.

In what follows, the design, prototyping and testing of a single-phase DM/CM separator, characterized by being easily extendable to the three-phase case, are described in detail.

4.1 Single phase splitter design

As known, the EMI noise generated by every device along its power lines can be decomposed in common mode and differential mode terms, taking as a reference the Protection Earth (PE) potential. Exploiting the definition, this concept can be depicted as in Figure 4.1(a), where equivalent DM and CM EMI noise generators are highlighted.
However, when employing a traditional measurement setup, which involve a LISN and a spectrum analyzer, just the signal present between each line and PE can be observed.

Therefore, if these virtual signal generators want to be "observed", an additional

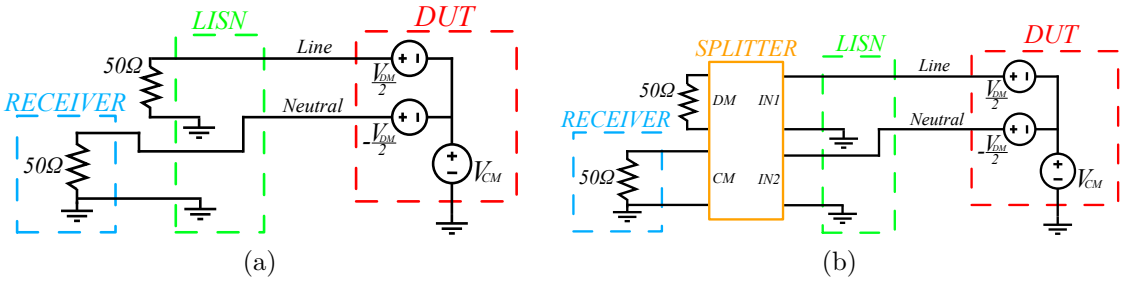

Figure 4.1: Equivalent high frequency circuit in a standard evaluation setup (a) and with the CM/DM separator (b).

device that separates the different contributions has to be introduced in between the LISN outputs and the EMC receiver (Figure 4.1(b)). To achieve this result, this device should simply implement the mathematical operations that define the two components. Another aspect that has to be taken into consideration by this object is the fact that each signal line of the LISN should be terminated with a 50Ω impedance to perform a correct measurement and this feature should be maintained.

To achieve these requirements the circuit of Figure 4.2 has been considered, where:

$$R_C = 25\Omega;\ R_{D1} = 50\Omega;\ R_{D2} = 50\Omega \tag{4.1}$$

NOTE: This circuit could be drastically simplified (the two branches at the secondaries of the transformers are in parallel). However, it has been chosen to keep

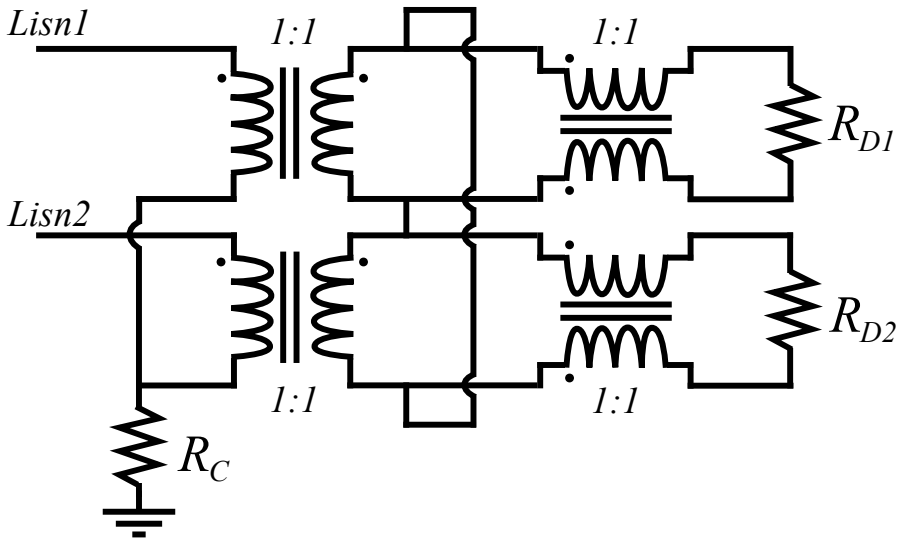

Figure 4.2: Structure of the single phase CM/DM splitter.

the structure and the idea behind it similar to that presented in [9], in order to highlight potential defects and criticalities, that could arise in the future three-phase implementation.

To analyze this structure and theoretically demonstrate its validity, we can consider the equivalent noise generator of Figure 4.1 and, exploiting superposition, we can derive the equivalent circuits seen respectively by CM and DM, reported in Figure 4.3.

Looking at the figure, it can be easily concluded that the signal seen on resistor R_C coincides with the CM noise, while the signal seen on R_{D1} and R_{D2} coincides with that generated by the two DM generators respectively. It can be noticed that R_{D1} and R_{D2} show the same potential (as they are actually in parallel), equal to $V_{DM}/2$. This is due to the fact that, according to the idea behind this circuit, each of the two resistors R_{D1} and R_{D2} carry the voltage of one of the two $V_{DM}/2$ generators of Figure 4.1. In a single phase system, these two signal are necessarily opposite and equal. However, this is not true in a three-phase system, where the condition for having a differential signal is that the *vector* sum of the 3 signals cancels out, therefore it becomes essential to keep the 3 components separated. In a single-phase analysis like this one, this fact could be considered unwanted, as typically the full V_{DM} signal is desired. However, since this study represents just

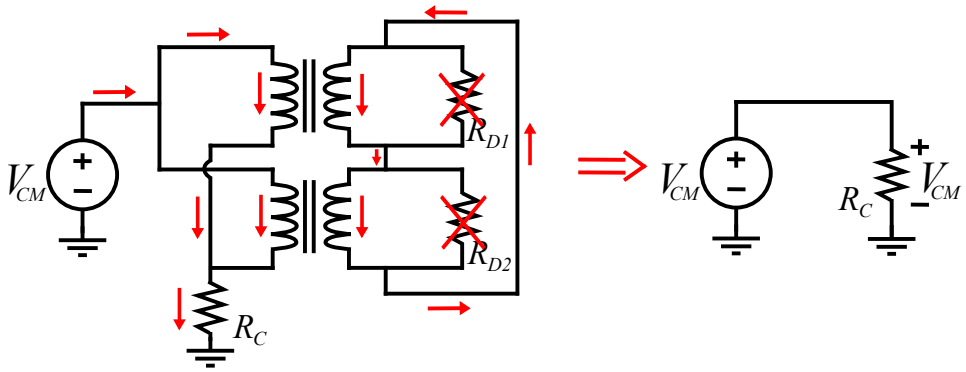

(a)

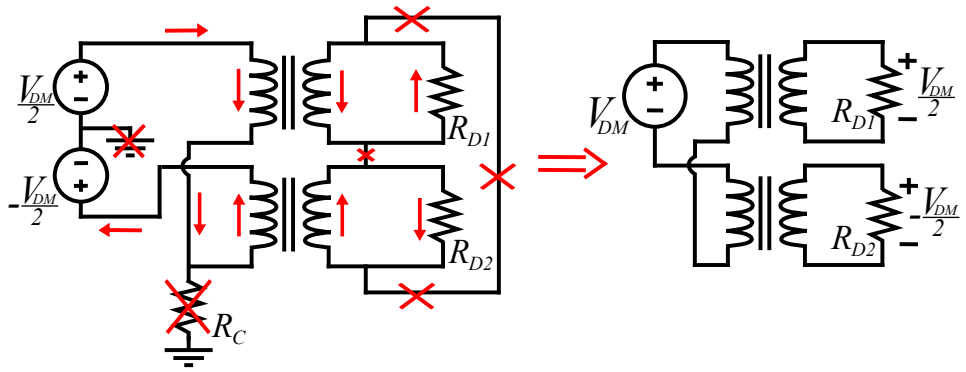

(b)

Figure 4.3: Signals paths and equivalent circuits for CM (a) and DM (b) (the CM-chokes have not been represented).

a preliminary investigation before the implementation of the three-phase version and since this fact would introduce just a $6dB$ offset, it has been accepted and not further discussed.

Finally, the other requirement for this device has to be verified, *i.e.* it has to show 50Ω impedance at each input port. To do that, a test generator is applied at one port, while the other one is grounded, like shown in Figure 4.4(a).

This circuit can be analyzed by decomposing the test generator V_t in its common mode and differential mode components, as done in Figure 4.4(b). In this way, the simplified schematics of Figure 4.3 can be exploited and the current through the test generator can be easily computed:

$$I_t = \frac{I_{cm}}{2} + I_{dm} = \frac{V_t/2}{2R_C} + \frac{V_t}{R_{D1}+R_{D2}} = \frac{V_t}{100\Omega} + \frac{V_t}{100\Omega} \implies Z_{in} \triangleq \frac{V_t}{I_t} = 50\Omega \quad (4.2)$$

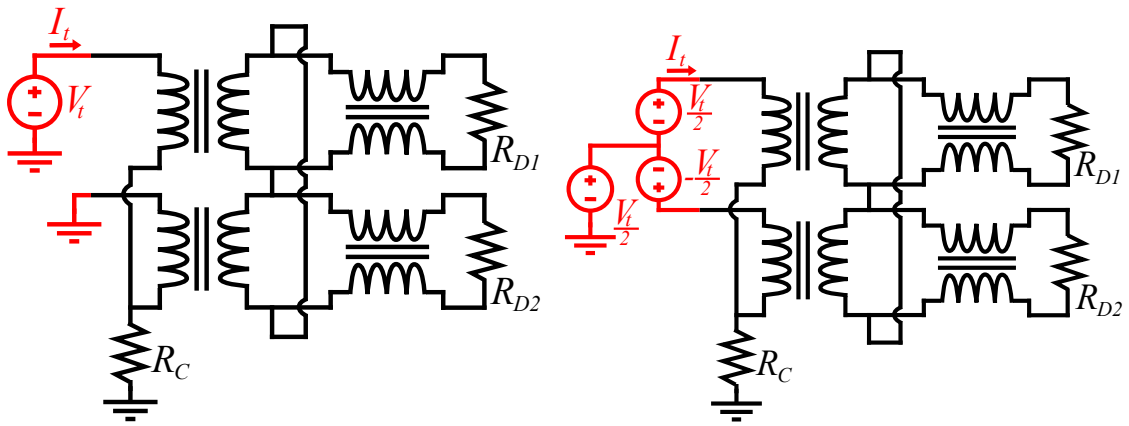

(a) (b)

Figure 4.4: (a) Circuit schematic for the input impedance verification, (b) its equivalent CM and DM representation.

Hence, this device actually shows a 50Ω impedance at its port, as desired. For symmetry, this is verified also for the other port.

Looking at Figure 4.2, it can be noticed the presence of two CM-chokes in the secondary side of the circuit.
These elements have been introduced since the various resistances can be practically implemented using BNC terminations or even using the input impedance of the receiver. In this last case, since one end of the input of the receiver is bounded to PE, this would introduce an additional CM path, that could compromise the measurements. These CM-chokes introduce an high CM impedance that breaks this path.

4.2 Practical implementation and tests

At this point, the structure described and analyzed in the previous section has been practically implemented in a prototype board. The final circuit is shown in Figure 4.5.

Since it is a circuit that operates at high frequency, particular attention was paid on keeping the connections as short as possible, as well as on maximizing the

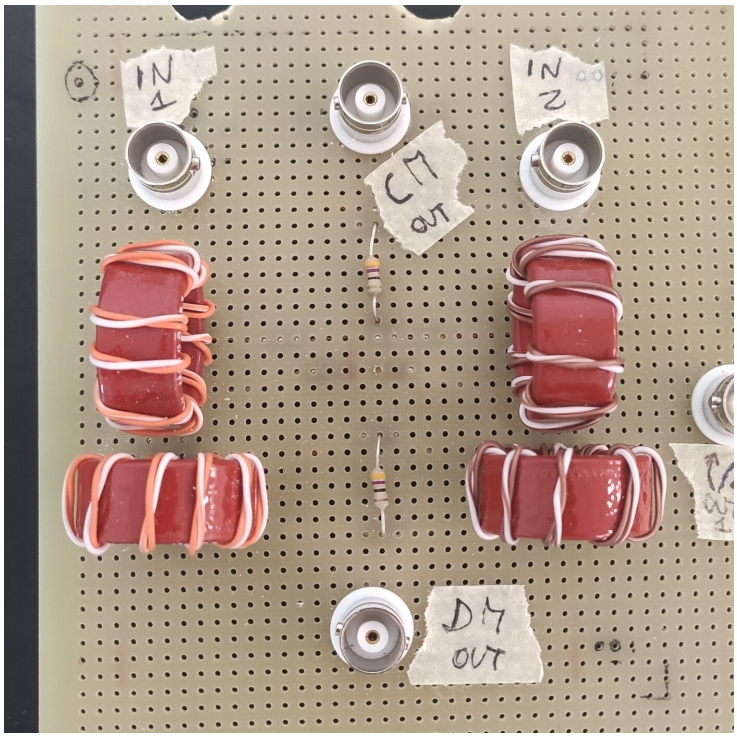

Figure 4.5: Photo of the CM/DM splitter prototype.

symmetry of the board.

In addition, great care has been paid in the realization of the transformers (especially because they make up most of the circuit).
First of all, the way the transformer is wound has been carefully evaluated. Indeed, parasitic components could drastically degrade the high frequency performance of the device, therefore they have to be minimized as much as possible. Hence, in Figure 4.6 two opposite winding methodologies are proposed.

In the first case the primary and secondary coils are kept well separated. This strategy minimizes the coupling capacitance between the two winding, but a very large leakage flux is generated. In the second case, instead, the opposite is done, in fact the two coils are very tightly wounded (even using a twisted pair). This solution allows to reduce leakage inductances, that would be responsible for a poor bandwidth, as confirmed looking at Figure 4.7 where these two approaches are tested. As can be seen, using a tight winding the bandwidth improves from about $700kHz$ to $20MHz$. Therefore, this winding methodology is preferable in our case.

(a) (b)

Figure 4.6: Two possible winding methodologies: (a) splitted and (b) tight winding.

In addition, a single layer winding has been realized in order to prevent layer-to-layer stray capacitance, while the individual turns are well separated from each other in order to reduce inter-winding capacitances.

Meanwhile, two available toroidal cores have been compared, one made of ferrite and the other made of a nanocrystalline material (Vitroperm 500 F). These two cores typologies are typically employed in CM-chokes realization, therefore high permeability and low losses are expected at high frequency. This makes them suitable for the purpose.
The results can be observed comparing the frequency response of the first core in Figure 4.8, with that of the second one already seen in Figure 4.7(b).
As can be observed, the nanocrystalline core shows much better performance at high frequency with respect to the ferrite one, whose bandwidth starts decreasing before $10MHz$. For this reason, the first core has been chosen for this work and will be considered in the following.
Finally, looking again at Figure 4.5, the 4 transformers have been placed well separated or, at least, orthogonally, in order to minimize the mutual magnetic coupling between them.

Then, once the prototype was realized, the capabilities of this device have been

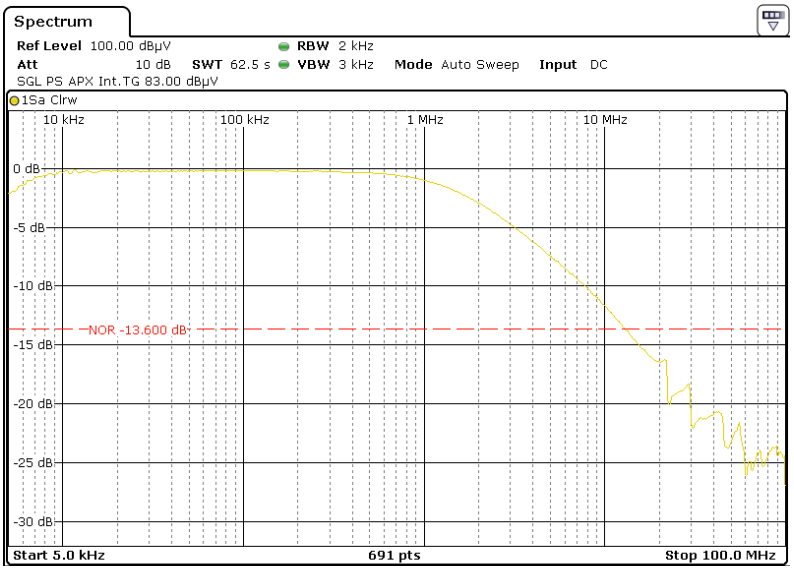

(a)

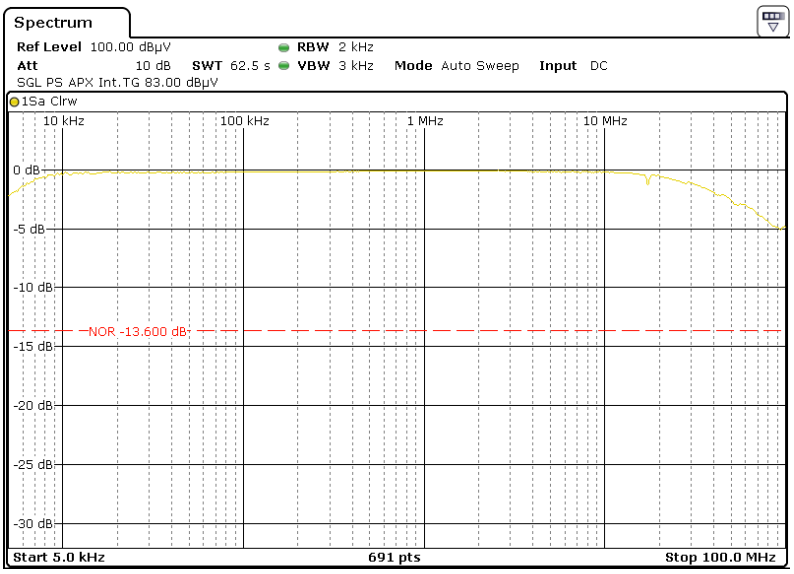

(b)

Figure 4.7: Bandwidths achieved using a nanocrystalline core and implementing (a) the winding technique of Figure 4.6(a) and (b) that of Figure 4.6(b).

evaluated by measuring the transmission transfer functions, applying a purely DM[CM] signal and looking at the DM[CM] output, and the rejection transfer functions, applying a purely DM[CM] signal and looking at the CM[DM] output. In order to apply a differential signal by means of a signal generator whose negative

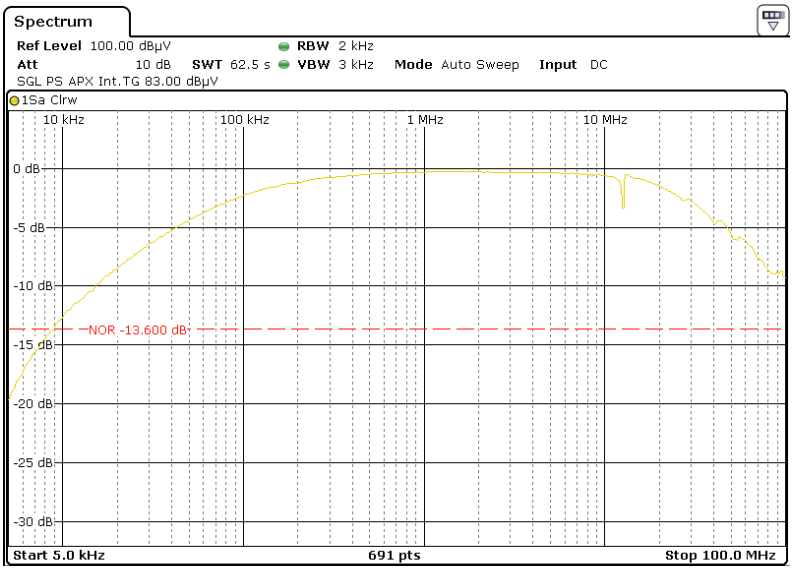

Figure 4.8: Bandwidth achieved using a ferrite core and tight winding.

end is bounded to PE, an isolation transformer has been introduced.
The result of these analysis are reported in Figure 4.9 for transmission functions and in Figure 4.10 for rejection functions.

Looking at rejection function we can conclude that the device behaves very well, especially at frequencies below $10MHz$ where an attenuation of at least $30dB$ is guaranteed for both cases.
Even considering transmission functions, nice results are observed, as the output signal starts decreasing above $20MHz$ for DM and above $30MHz$ for CM.
It can be noticed that these plots include an unexpected offset of about $3.5dB$. This is due to the voltage divider generated between the 50Ω source impedance of the signal generator Z_g and the equivalent load impedance of the device Z_l. Looking at Figure 4.3 it can be concluded that the equivalent load impedances are 25Ω for CM and 100Ω for DM. Therefore, recalling the fact that the instrument shows $0dB$ when it is loaded with 50Ω (in other words, it automatically shifts the trace by $6dB$), for CM we get:

$$A^{cm} = 20log\left(\frac{Z_l^{cm}}{Z_l^{cm} + Z_g}\right) + 6dB = -3{,}54dB\ . \tag{4.3}$$

For DM we should also consider that the output signal is half of the generated one,

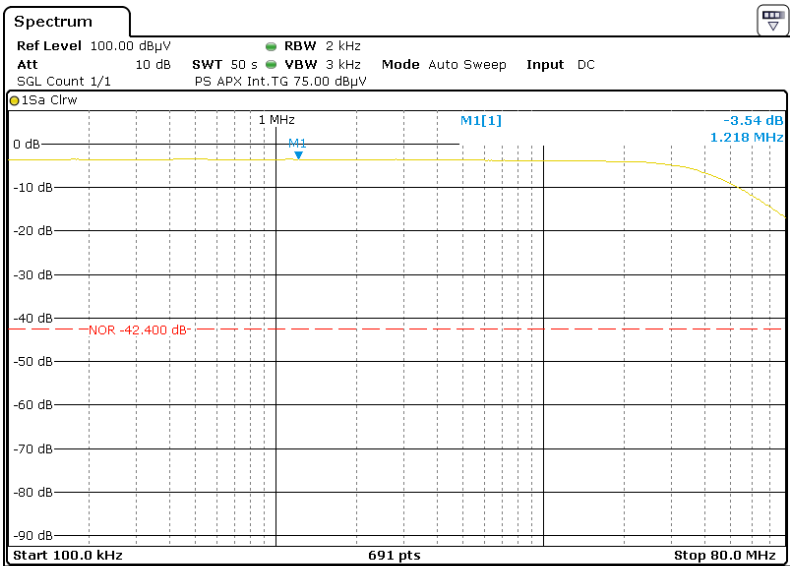

(a)

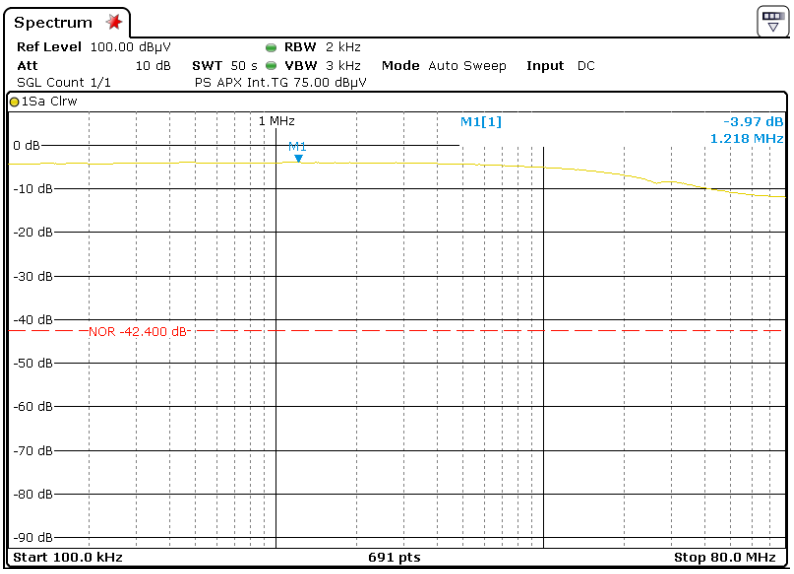

(b)

Figure 4.9: Transmission functions obtained applying a CM or DM signal and observing the output of the same mode: (a) is CM and (b) is DM.

for the reasons already explained. Therefore:

$$A^{dm} = 20log\left(\frac{Z_l^{dm}}{Z_l^{dm} + Z_g} * \frac{1}{2}\right) + 6dB = -3{,}54dB \tag{4.4}$$

These results are consistent with the observed offsets.

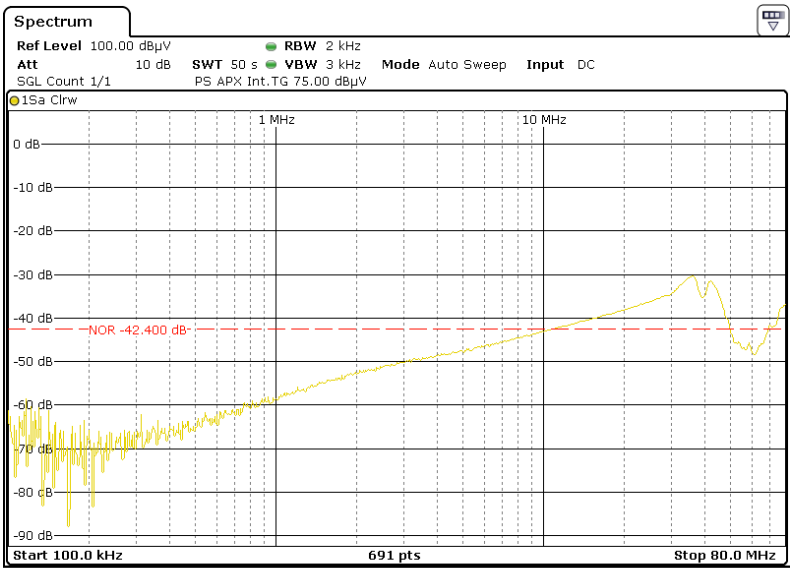

(a)

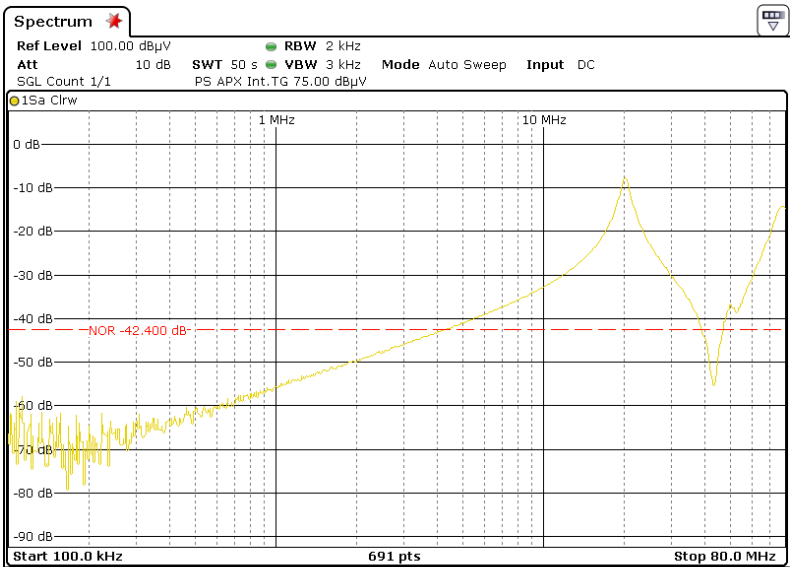

(b)

Figure 4.10: Rejection functions obtained applying a CM signal and looking at the DM output (a) and vice versa for (b).

At this point, the operation of this device can be verified also in an actual practical case, as depicted in Figure 4.1(b).
However, before doing this, it has been necessary to adapt a LISN for this purpose.

In fact, typically, a LISN does not provide to the user all the noise signals simultaneously, but only a single output, that can be switched between the different lines by means of a button. Therefore, a three-phase LISN has been disassembled, the commutation circuit has been bypassed and the 4 noise signals have been made accessible from the front panel with BNC connectors (Figure 4.11).

Now it is possible to introduce the CM/DM separator in the setup, between the

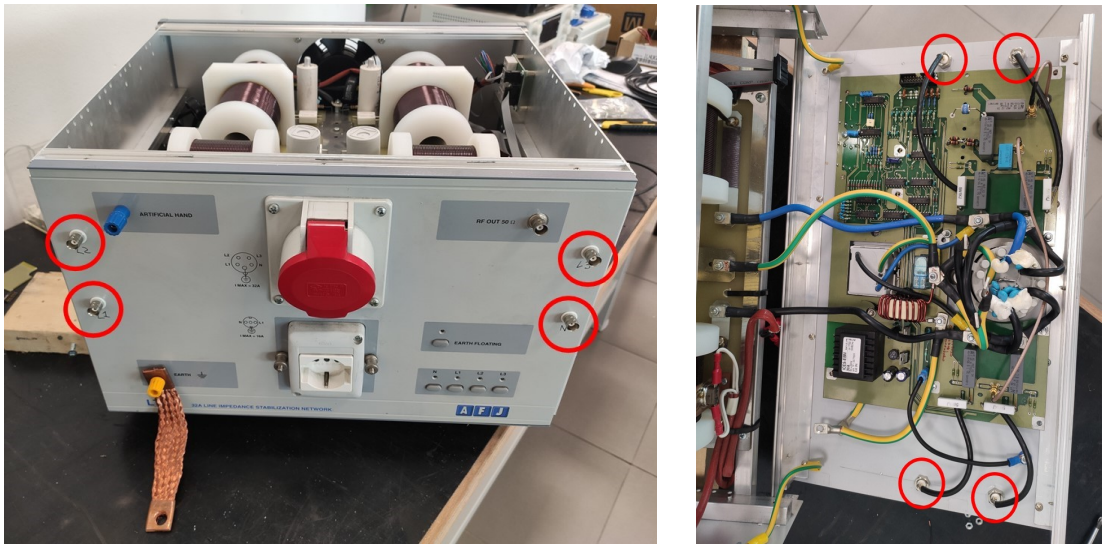

Figure 4.11: LISN adjustments to bypass the commutation circuit and provide the 4 noise signals in the 4 BNC connectors.

LISN and the EMC receiver. As a noise source, the inverter's power supply considered also in Section 3.3.2 has been used.
In Figure 4.12 the two output of the CM/DM splitter are reported.

Unfortunately there was no possibility to verify the quality of the results, however it can be observed that they are consistent with those expected recalling the reasoning done in the second chapter of [7] *i.e.* DM noise firstly decreases as $1/f$ and then, after a certain frequency, it remains constant, while CM noise should be almost constant around the whole EMI spectrum.

In conclusion, we can say that this device behaves very well and can be considered reliable up to $10MHz - 20MHz$. This is sufficient to exploit this tool in the AEF analysis, since, as known, their effect is typically limited to frequencies below

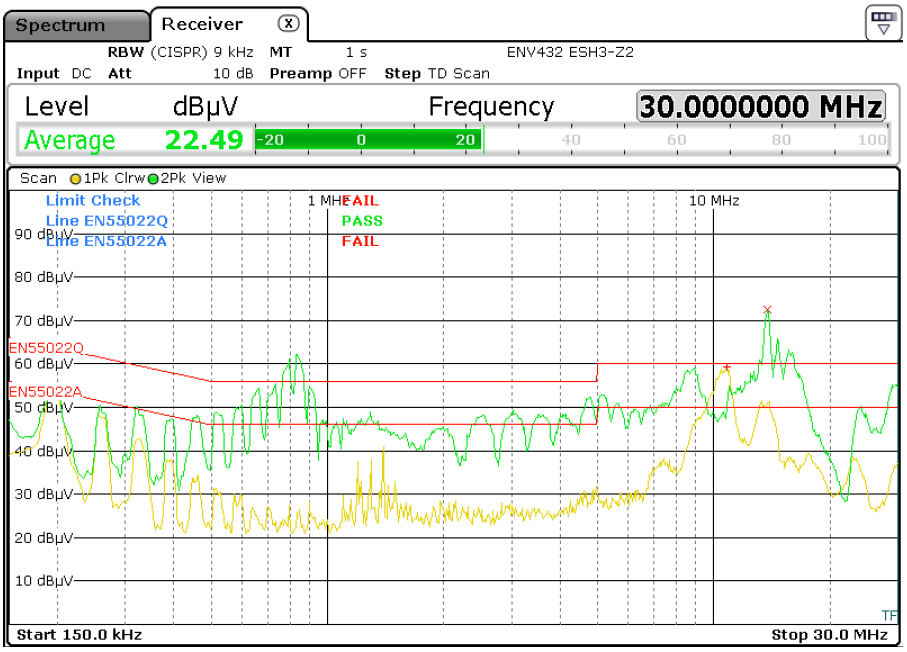

Figure 4.12: Outputs of the CM/DM splitter: in green the CM signal, in yellow half of the DM signal.

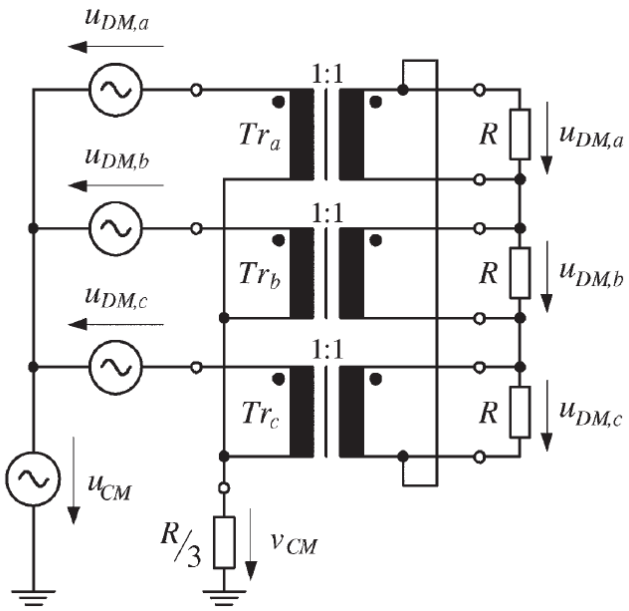

Figure 4.13: Three-phase version of the CM/DM splitter [9].

a few MHz.

Many additional precautions can be taken in order to further improve the performance of this device. For instance, the circuit can be realized in a properly designed PCB, which would further minimize parasitic effects, or more refined HF transformers can be considered. The whole system should also be enclosed in a metallic case, which would introduce a shielding from external interference.
Anyway, in this case, the result has been considered sufficient to demonstrate the effectiveness of this structure and its suitability for the three-phase version whose structure has been reported in Figure 4.13 and whose behavior is well explained in [9].

Chapter 5

Conclusions

This document summarizes my experience carried out at the DELIOS company in Cittadella, specialized in the development of photovoltaic inverters, which hosted and supported me during this period.

In this work, a comprehensive study about the application of an active filter in the EMI field was conducted. The filter has been analyzed in depth, demonstrating its functioning and effectiveness, and the design process was also illustrated. The developed circuit was finally practically implemented in a prototype and experimentally tested.
The considered approach is different from that generally used. Indeed, the necessity to introduce the device in an industrial context has guided various choices and the evaluation of the results. Cost, availability of components and repeatability of results played a crucial role in defining the project.
Practical tests have demonstrated the actual effectiveness of this technology, showing an improvement in attenuation of up to $20dB$.

The developed circuit was then compared with an integrated solution provided by Texas Instruments. The idea was to define the performance improvement allowed by the integrated technology, guaranteed by the extreme minimization of parasitic components and component variability, crucial aspects in the EMI frequency range.
However, surprisingly, in the two practical cases considered, the integrated circuit proved to be significantly inferior compared to the homemade one.

Other critical issues related to the application of this Integrated Circuit have been identified. In particular, the fact that this component represents the only option of this type available on the market represents a terrible aspect at an industrial level, as component availability crises (such as the one faced in recent years) can seriously compromise the production and marketing of the device. On the other hand, the discrete solution would be certainly much less troublesome from this point of view. However, if this technology begins to be appreciated and become popular, there is no doubt that many other manufacturers would enter this area, and this would make the integrated option much more considerable.

Finally, the introduction of the two circuits in a much more complex system than that of the previous tests, *i.e.* the output of a hybrid PV inverter, made it possible to point out a limitation of this solution, that is versatility.
In fact, if a normal passive EMI filter can be designed in a reliable way quite immediately, exploiting known structures and robust components, this cannot be said for the active filters, whose compensation network must be carefully defined case by case and, as in the considered case, this may not be trivial.

Overall, the use of an active EMI filter is certainly an interesting technology, the effectiveness of which has been widely demonstrated, although a considerably greater effort in the design phase must be taken into account. However, this seems to be necessary if maximum compactness in the finished product has to be achieved.

Simultaneously with the main work, the development of a CM/DM splitter has been carried out.
The considered structure has been analyzed and evaluated both theoretically and experimentally. A prototype of this circuit has been carefully implemented, which allowed to confirm its validity for a future three-phase realization and also turned out very useful in the experimental analysis of the AEF.

Bibliography

[1] M.Bertocco A.Sona. *Manuale di Compatibilita' Elettromagnetica*. 2nd. ISBN: 978-1-326-04760-3. 2010.

[2] Alessandro Amaducci. "Design of a wide bandwidth active filter for common mode EMI suppression in automotive systems". In: *2017 IEEE International Symposium on Electromagnetic Compatibility and Signal/Power Integrity (EMCSI)*. 2017, pp. 612–618. DOI: 10.1109/ISEMC.2017.8077941.

[3] Frede Blaabjerg. *Control of Power Electronic Converters and Systems, Volume 2*. 2nd. ISBN: 978-0-128-16136-4. Elsevier Science Publishing Co Inc, 2018.

[4] A. Charoy. "Electromagnetic Compatibility of Power Converters". In: (July 2016). DOI: 10.5170/CERN-2015-003.83.

[5] Wenjie Chen, Xu Yang, and Zhaoan Wang. "An experimental study and comparison of common mode and differential mode noise compensation characteristic for active EMI filter". In: *2008 IEEE Power Electronics Specialists Conference*. 2008, pp. 4399–4404. DOI: 10.1109/PESC.2008.4592654.

[6] Maria Carmela Di Piazza, Antonella Ragusa, and Gianpaolo Vitale. "An Optimized Feedback Common Mode Active Filter for Vehicular Induction Motor Drives". In: *IEEE Transactions on Power Electronics* 26.11 (2011), pp. 3153–3162. DOI: 10.1109/TPEL.2011.2147801.

[7] B.Revol F.Costa E.Laboure. *Electromagnetic Compatibility in Power Electronics*. ISBN: 978-1-848-21504-7. Wiley-ISTE, 2014.

[8] Djilali Hamza, Majid Pahlevaninezhad, and Praveen K. Jain. "Implementation of a Novel Digital Active EMI Technique in a DSP-Based DC-DC Digital

Controller Used in Electric Vehicle (EV)". In: *IEEE Transactions on Power Electronics* 28.7 (2013), pp. 3126–3137. DOI: 10.1109/TPEL.2012.2223764.

[9] M. L. Heldwein et al. "Novel Three-Phase CM/DM Conducted Emission Separator". In: *Industrial Electronics, IEEE Transactions on* 56 (Oct. 2009), pp. 3693–3703. DOI: 10.1109/TIE.2009.2025287.

[10] Marcelo Lobo Heldwein. "EMC Filtering of Three-Phase PWM Converters". PhD thesis. Federal University of Santa Catarina, 2008.

[11] Marcelo Lobo Heldwein et al. "Implementation of a Transformerless Common-Mode Active Filter for Offline Converter Systems". In: *IEEE Transactions on Industrial Electronics* 57.5 (2010), pp. 1772–1786. DOI: 10.1109/TIE.2009.2032204.

[12] Marcelo Lobo Heldwein et al. "Implementation of a Transformerless Common-Mode Active Filter for Offline Converter Systems". In: *IEEE Transactions on Industrial Electronics* 57.5 (2010), pp. 1772–1786. DOI: 10.1109/TIE.2009.2032204.

[13] Texas Instruments. *TPSF12C1-Q1 Datasheet*. [Online] https://www.ti.com/lit/ds/symlink/tpsf12c1-q1.pdf?ts=1699054104753&ref_url=https%253A%252F%252Fwww.ti.com%252Fproduct%252FTPSF12C1-Q1.

[14] Cornelis J.Kikkert. *RF Electronics Design and Simulation*. 1st. ISBN: 978-0-9873109-3-4. James Cook University, 2013.

[15] Sangyeong Jeong, Dongil Shin, and Jingook Kim. "A Transformer-Isolated Common-Mode Active EMI Filter Without Additional Components on Power Lines". In: *IEEE Transactions on Power Electronics* 34.3 (2019), pp. 2244–2257. DOI: 10.1109/TPEL.2018.2845467.

[16] Sangyeong Jeong, Dongil Shin, and Jingook Kim. "A Transformer-Isolated Common-Mode Active EMI Filter Without Additional Components on Power Lines". In: *IEEE Transactions on Power Electronics* 34.3 (2019), pp. 2244–2257. DOI: 10.1109/TPEL.2018.2845467.

[17] Junpeng Ji et al. "Delay and Decoupling Analysis of a Digital Active EMI Filter Used in Arc Welding Inverter". In: *IEEE Transactions on Power Electronics* 33.8 (2018), pp. 6710–6722. DOI: 10.1109/TPEL.2017.2758682.

[18] Sangyeong Jeong Jingook Kim. *Passive and Active EMI FIlters for Power Electronics*. [Online] https://www.youtube.com/watch?v=pMRwKUlBq5E&t=1483s.

[19] L.Rossetto. *Appunti dal corso di elettronica analogica*. 2nd. ISBN: 978-8-874-88991-4. 2016.

[20] Krishna Mainali and Ramesh Oruganti. "Conducted EMI Mitigation Techniques for Switch-Mode Power Converters: A Survey". In: *IEEE Transactions on Power Electronics* 25.9 (2010), pp. 2344–2356. DOI: 10.1109/TPEL.2010.2047734.

[21] Illia Manushyn. "Design and Optimization of EMI Filters for Power Electronics Systems". PhD thesis. Technische Universitat Darmstadt, 2018.

[22] Balaji Narayanasamy, Fang Luo, and Yongbin Chu. "Modeling and Stability Analysis of Voltage Sensing based Differential Mode Active EMI Filters for AC-DC Power Converters". In: *2018 IEEE Symposium on Electromagnetic Compatibility, Signal Integrity and Power Integrity (EMC, SI & PI)*. 2018, pp. 322–328. DOI: 10.1109/EMCSI.2018.8495239.

[23] R.D.Middlebrook. "Measurement of Loop Gain in Feedback Systems". In: *Int. J. Electronics* 38.4 (1975), pp. 485–512.

[24] Lon M. Schneider. "Noise Source Equivalent Circuit Model for Off-Line Converters and its use in Input Filter Design". In: *1983 IEEE International Symposium on Electromagnetic Compatibility*. 1983, pp. 1–9. DOI: 10.1109/ISEMC.1983.7567390.

[25] Dongil Shin et al. "Analysis and Design Guide of Active EMI Filter in a Compact Package for Reduction of Common-Mode Conducted Emissions". In: *IEEE Transactions on Electromagnetic Compatibility* 57.4 (2015), pp. 660–671. DOI: 10.1109/TEMC.2015.2401001.

[26] Dongil Shin et al. "Analysis and Design Guide of Active EMI Filter in a Compact Package for Reduction of Common-Mode Conducted Emissions". In: *IEEE Transactions on Electromagnetic Compatibility* 57.4 (2015), pp. 660–671. DOI: 10.1109/TEMC.2015.2401001.

[27] Y.-C. Son and Seung-Ki Sul. "Generalization of active filters for EMI reduction and harmonics compensation". In: *IEEE Transactions on Industry Applications* 42.2 (2006), pp. 545–551. DOI: 10.1109/TIA.2006.870030.

[28] Dongbing Zhang. “Switching mode power supply noise source impedance measurement and EMI filter characterization”. PhD thesis. Virginia polytechnic institute, 1996.